7. Česko-Slovenská studentská vědecká konference ve fyzice
Fakulta jaderná a fyzikálně inženýrská
České vysoké učení technické v Praze
23. – 24. května 2016

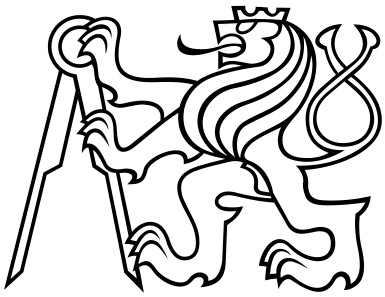

Production of J/ψ meson in central U+U collisions at the STAR experiment

Jana Fodorová

Department of Phyiscs
Faculty of Nuclear Sciences and Physical Engineering
Czech Technical University in Prague

Abstract

Under normal conditions the basic building blocks of matter, quarks and gluons, are bound within hadrons. The theory of strong interaction predicts a phase transition at high temperature and energy density from hadronic matter to the state of deconfined quarks and gluons called quark-gluon plasma (QGP). It is expected that heavy-ion collisions at the Relativistic Heavy Ion Collider (RHIC) in Brookhaven National Laboratory achieve conditions needed for the QGP formation. The suppression of production of bound states of heavy quarks (c, b) and their antiquarks, heavy quarkonia (e.g. J/ψ), due to the color screening of the quark-antiquark potential in the deconfined medium has been proposed as a signature of the QGP. However, other effects such as secondary production in the QGP complicate the suppression picture. We describe the analysis of J/ψ production via the di-electron decay channel in 0-5 % most central U+U collisions at $\sqrt{s_{\mathrm{NN}}} = 193$ GeV at the STAR experiment at RHIC. Preliminary results on invariant yield and nuclear modification factor of J/ψ are presented.

Key words: quark-gluon plasma, heavy-ion collisions, RHIC, heavy quarkonia, J/ψ

Content of this work

This work includes and summarizes different parts of author's diploma thesis. The thesis was carried out under the supervision of RNDr. Petr Chaloupka, Ph.D. and consulted with Mgr. Jaroslav Bielčík, Ph.D. Presented analysis and preliminary results were discussed with members of the heavy flavor physics working group of The STAR Collaboration.

Contents

List of Figures

List of Tables

Chapter 1

Heavy quarkonia in heavy-ion collisions

One of the most important and "always up-to-date" challenges of physics is the understanding of the laws of the world and the Universe and finding out what it consists of. In a more fundamental sense, the basis of this study is the determination what the elementary building blocks of matter are and how they interact with each other.

A very successful theory in this field is the Standard Model of particle physics developed during the second half of the 20th century. It is a quantum field theory concerning the electromagnetic, weak and strong interactions, as well as elementary particles classified into quarks (u, d, s, c, b, t), leptons $(e, \nu_e, \mu, \nu_\mu, \tau, \nu_\tau)$ and bosons $(\gamma, W, Z$, gluons and Higgs boson).

The strong interaction is responsible for binding quarks and gluons into hadrons (protons, neutrons) and, on a larger scale, protons and neutrons into nuclei. The theory of Quantum Chromodynamics (QCD) is used to describe the strong force between quarks (antiquarks) mediated by gluons. In this theory each quark (antiquark) carries one of three color charges: red, green, blue (antired, antigreen, antiblue). Quarks bind through the strong interaction to form color-neutral bound states, the already mentioned hadrons. Hadrons are known as mesons if they are made up of a quark of some color and an antiquark with corresponding anticolor, or as baryons if they are formed from three quarks or antiquarks with all three colors or anticolors.

The QCD coupling constant α_s which determines the strength of the strong interaction is proportional to [1]

$$\alpha_s(Q^2) \sim \frac{1}{ln(\frac{Q^2}{\Lambda^2_{QCD}})} \tag{1.1}$$

where Λ_{QCD} is the QCD scale and Q denotes the momentum transfer in the interaction. At low Q^2 the coupling constant α_s is large and the QCD potential can be approximated by [2]

$$V(r) \approx kr \tag{1.2}$$

where k is constant called string tension. Hence the attractive force between quark and antiquark increases with distance r. When the QCD potential is high enough the string breaks and a new quark-antiquark pair is created out of the vacuum. Accordingly, it is not possible to observe free quark or gluon, free color charge. This characteristic feature of the QCD is called color confinement. On the other hand, with increasing Q^2 and decreasing the interaction distance α_s decreases. Under extreme conditions, at asymptotically small distances or high Q^2 α_s gets very small and quarks can be treated as free particles. This phenomenon is called asymptotic freedom.

The phase of matter consisting of asymptotically free quarks and gluons is called quark-gluon plasma (QGP). It is believed that the Universe was in this state for about few milliseconds after the Big Bang. Currently, there is a large experimental effort to create the QGP and to study its properties. At present, the only way of testing it, is in heavy-ion collisions.

1.1 Heavy-ion collisions

High temperatures and energy densities reached in ultrarelativistic heavy-ion collisions allow to study properties of the nuclear matter at such extreme conditions that the transition of hadronic nuclear matter into the state of asymptotically free quarks and gluons takes part.

Currently, the main goal of colliding ultrarelativistic heavy ions is to precisely study the transition of the hadronic matter into the state of deconfined quarks and gluons as well as properties of the medium formed in the collisions.

1.1.1 Space-time evolution of the heavy-ion collision

Nucleus-nucleus collisions have long been the object of study of many physicists, however, even today it is not known exactly how the ultrarelativistic heavy-ion collision occurs. Here, the possible scenario of the heavy-ion collision is briefly described (see Figure 1.1 where also the evolution without the QGP phase is illustrated).

Immediately after the collision nuclei traverse each other depositing a large amount of energy in the medium in the form of excited virtual quanta. As a result of their deexcitation quarks and gluons are created and interact with each other.

As the system reaches the thermal equilibrium it can be described by the laws of hydrodynamics. From this moment it is in the quark-gluon plasma phase. The proper time of the system when it enters this phase is estimated to be $\tau_0 \leq 1$ fm/c [3]. The system expands and cools down. When the critical temperature $T_c \simeq 170$ MeV [3] is reached, quarks and gluons can no longer be free within the system and are confined into hadrons. However, it is not clear if the phase transition into the hadron gas happens immediately or if it is proceeded by the mixed phase of quarks, gluons and hadrons.

As the system is in the phase of hadron gas, it cools down and expands until the chemical freeze-out begins.

During the chemical freeze-out inelastic scatterings between the hadrons disappear and the particle identities are set. However, hadrons can still interact elastically. Elastic collisions disappear at thermal freeze-out. At the end, hadrons fly out to the detector.

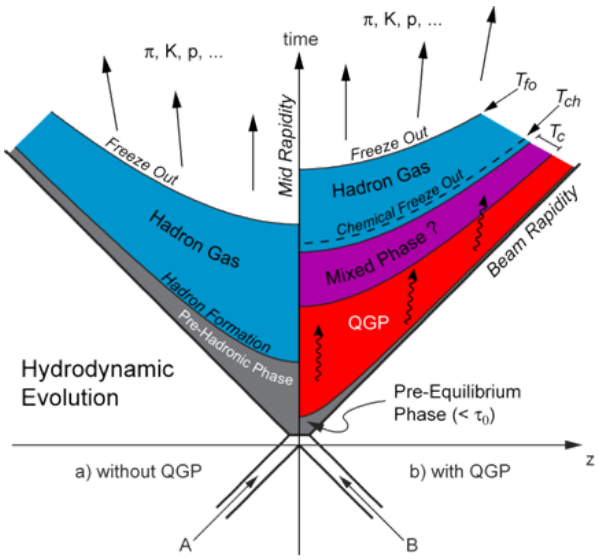

Figure 1.1: Two scenarios of the evolution of the relativistic collision – without and with the presence of the QGP phase [4].

1.1.2 Centrality of the collision

As in every experiment the initial conditions are very important. This applies particularly for collisions of heavy nuclei. They can be classified according to different criteria, such as the size and type of colliding nuclei or the energy of the collision. In order to study effects of the medium created in the ultrarelativistic collisions of heavy-nuclei it is useful to sort collisions according to the size of the overlapping area of the colliding nuclei. As the overlap is larger, there are more nucleons which can participate in interactions thus the energy density of the medium can be higher. This can turn into higher probability of the QGP formation.

Based on the size of the overlapping area the collisions of heavy nuclei can be divided into central, peripheral or ultra-peripheral. There are two experimental ways which are often used to measure the collisional centrality. The centrality can be determined by measuring the spectators − nucleons which do not participate in interactions. At the STAR experiment, they are measured by the so called Zero Degree Calorimeters [5]. One could expect that as the number of spectators decreases the centrality increases. However, not only for the most central but also for the most peripheral collisions the number of spectators is ~ 0 since nucleons of the colliding nuclei are not kicked out of the nuclei and, therefore, not measured by ZDCs. Moreover, different orientations of the deformed nuclei at the same impact parameter can turn into different number of measured spectators. Therefore, this method of centrality definition is not unambiguous. Another way of accessing the information abot centrality of the collision is by the track multiplicity measurements − more central collisions mean more nucleons participating in the collision which turn to higher multiplicity − more tracks observed in the detector. Figure 1.2 shows the charged particle multiplicity N_{ch} distribution and its relation to centrality classes or the number of participating nucleons in the collision N_{part}.

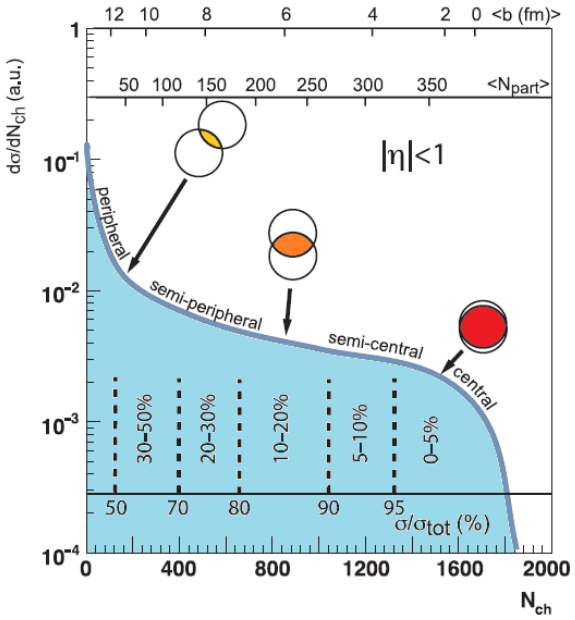

Figure 1.2: The charged particle multiplicity N_{ch} distribution and corresponding centrality classes [6].

1.1.3 U+U Collisions

Collisions of deformed nuclei provide an opportunity to study the spatial dependence of various properties and effects of the created. Within the same colliding system, deformed nuclei

can have different spatial orientations and, therefore, allow wider variations of energy density of the created medium. The study of deformed nuclei is also supported by theoretical expectations of higher energy density reached compared with collisions of spherical nuclei, namely in the case of U+U compared with Pb+Pb collisions [7] and Au+Au collisions [8].

In 2012 prolate U nuclei were collided at RHIC at $\sqrt{s_{\mathrm{NN}}} = 193$ GeV. Compared with symmetric Au nuclei being colided at RHIC, the orientation-averaged energy density reached in U+U collisions is expected to be up to 20% higher and for "tip+tip" configurations even more, up to 30% [8]. This is illustrated in the Figure 1.3 which shows the ratio of estimated energy densities in U+U and Au+Au collisions as a function of centrality. In the most central U+U collisions, the increase of the energy density is the highest hence in these collisions the most significant effects of the hot medium are expected to be present. Therefore, detailed study of the most central U+U collisions can provide a valuable information about the QGP.

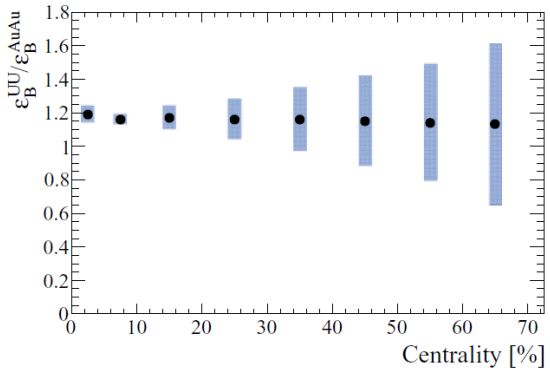

Figure 1.3: Ratio of expected energy density reached in U+U and Au+Au collisions ${\epsilon_{\mathrm{B}}}^{UU}/{\epsilon_{\mathrm{B}}}^{AuAu}$ as a function of centrality [8].

1.2 Heavy quarkonia

Due to their large masses heavy quarks (c, b) are produced in the initial hard interactions of partons in the earliest stages of the collisions. Since they experience the whole evolution of the system the information about the heavy quark production, its modification and collective flow can provide an insight into the thermodynamic properties and dynamics of the hot medium.

Heavy quarks can be investigated via open heavy flavor mesons (containing one heavy quark) or heavy quarkonia.

Opposite to open heavy flavor mesons containing one heavy quark, heavy quarkonia are often called hidden flavor as they are bound states of heavy quark (c, b) and its antiquark $(\bar{c}, \bar{b})$. According to the flavor content they are called charmonia $(c\bar{c})$ or bottomonia $(b\bar{b})$. The lightest vector charmonium, J/ψ, is the main object to study in this work.

1.2.1 Modification of heavy quarkonium production in heavy-ion collisions

Suppression of heavy quarkonium production in ultrarelativistic heavy-ion collisions compared with p+p collisions due to the color screening of quark-antiquark potential was proposed as one of the most prominent predictions about the QGP formation [9]. However, different other processes may contribute to the observed quarkonium yields and complicate the suppression picture, e.g. cold-nuclear-matter effects (nuclear shadowing, Cronin effect, nuclear absorption) or comover interactions which may be present also in the collisions in which the QGP is not expected to be formed (proton+nucleus collisions). For these reasons it is necessary to study heavy quarkonia in different colliding systems, at different centralities and collision energies.

Modification of heavy quarkonium production in nucleus+nucleus collisions compared with p+p collisions is usually quantified by the so-called nuclear modification factor R_{AA}. It is defined as the ratio of the number of particles produced in p+p collisions scaled by the average number of binary nucleon-nucleon collisions $< N_{\mathrm{bin}} >$. With no medium effect, the yield of heavy quarkonia in heavy-ion collisions should scale with the number of elementary collisions and R_{AA} should be equal to unity. As it turns out, the medium produced in havy-ion collisions can modify this scaling resulting in the effect of enhanement $R_{\mathrm{AA}} > 1$ or suppression $R_{\mathrm{AA}} < 1$.

Two often considered effects on quarkonium production in heavy-ion collisions are briefly described in following sections.

Dissociation due to the color screening

The prediction of the suppression of heavy quarkonium suppression in the deconfined medium is based on the idea that if the quarkonium is placed in the quark-gluon plasma of sufficient temperature $T > T_{\mathrm{C}}$, deconfined quarks and gluons will shield the color charge, effectively weaken the interaction between heavy quarks, string tension between them will vanish and they will no longer form a bound state.

In the QGP of the temperature T the quarkonium potential can be approximately expressed by the formula [9] :

$$V\left(r,T\right) = -\frac{\alpha}{r} exp\left[-r/r_D(T)\right], \tag{1.3}$$

where r is the radius of quarkonium and r_{D} is the Debye screening radius which sets the distance outside of which the color charge of heavy quark is screened, illustrated in Figure 1.4. The Debye

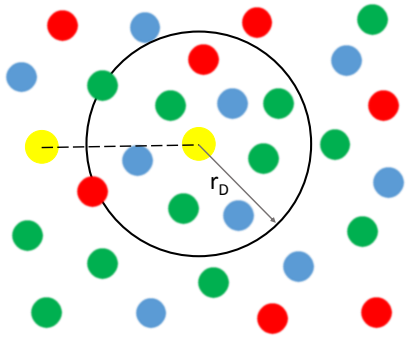

Figure 1.4: The schematic drawing of the Debye screening radius r_{D} in QGP. Heavy quarks from quarkonium (yellow) effectively do not see each other.

screening radius goes down with the increase of the temperature of the medium (approximately as $\sim 1/\sqrt{T}$ [10]). The temperature at which r_{D} decreases to the quarkonium radius r is the dissociation temperature T_{D} at which the quarkonium can no longer form a bound state. Since the radii of quarkonium states differ they are expected to dissociate at different temperatures. Therefore, it has been predicted that by measuring the states that survived in the QGP the information about the temperature of the medium could be obtained [10]. However, formula presented above is very approximate. There are different potential models (some of them were proposed also in [10]) and lattice QCD calculations which try to describe quarkonium dissociation mechanism.

Recombination

Suppression of heavy quarkonium production in QGP due to the melting can be compensated by the recombination of single thermalized heavy quarks. J/ψs produced from dissociated charm quarks are, in comparison to initially produced J/ψs from hard processes, are predicted to be distributed only in the low-p_{T} region.

The evidence of recombination effect can be observed from comparison of modification of J/ψ production at RHIC and LHC. This is illustrated in Figure 1.5 which shows J/ψ R_{AA} measured at PHENIX and ALICE at forward rapidity. At LHC where much higher energy of the collisions are reached the suppression of J/ψ as a function of N_{part} is lower than at RHIC and does not depend very much on centrality [11]. This result favors the scenario of more significant effect of recombination compared with melting at LHC energies than at RHIC.

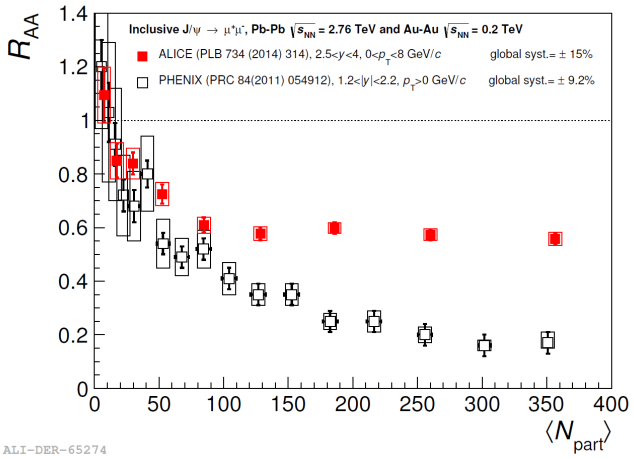

Figure 1.5: J/ψ R_{AA} as a function of N_{part} at PHENIX and ALICE at forward rapidity [11].

1.2.2 Heavy quarkonium measurements in heavy-ion collisions at RHIC

At RHIC the heavy quarkonium studies focus on a variety of measurements of J/ψ and Υ mesons in collisions of different nuclei such as Cu+Au, Au+Au and U+U. These colliding systems allow to study the QGP effects and their dependence on the energy density of the medium created in the evolution of the collision.

Results from Au+Au collisions

Figure 1.6 shows the nuclear modification factor R_{AA} as a function of number of participating nucleons N_{part} in the collision of high-p_{T} J/ψ together with low-p_{T} data. As can be seen, low-p_{T} J/ψ are more suppressed than high-p_{T} J/ψ over the whole N_{part} range. However, suppression of high-p_{T} J/ψ in central collisions is also significant. These results are consistent with model predictions [12] which include suppression of J/ψ production due to the color screening and statistical regeneration as a secondary production mechanism. Since regeneration is more significant at low-p_{T} high-p_{T} J/ψ can serve as a cleaner probe of suppression effects of the hot medium.

Results from U+U collisions

Measurements of J/ψ in U+U collisions provide an opportunity to prove the expected increase of the energy density of the medium up to above 20 % compared with Au+Au collisions.

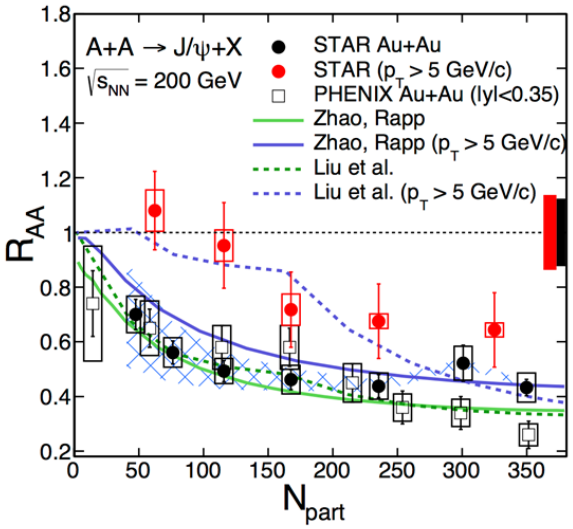

Figure 1.6: J/ψ nuclear modification factor $R_{\rm AA}$ in 200 GeV Au+Au collisions as a function of number of participant nucleons $N_{\rm part}$. Data are from STAR [13, 14] and PHENIX [15] and compared to model calculations [12, 16].

Increase of the energy density can affect resulting $R_{\rm AA}$ in several ways: on one hand, it can intensify the effect of color screening on the other hand, higher energy density means higher probability of J/ψ production via the coalescence of unbound $c\bar{c}$ pairs. Results on modification of J/ψ production in Au+Au collisions at various energies indicated possible interplay of melting and recombination.

Figure 1.7 shows preliminary results on J/ψ nuclear modification factor in minimum-bias and HT triggered U+U collisions at mid-rapidity at $\sqrt{s_{\rm NN}} = 193$ GeV at STAR. In the left panel U+U data are compared to 200 GeV Au+Au $R_{\rm AA}$ as a function of $p_{\rm T}$ while the right panel shows $N_{\rm part}$ dependence of $R_{\rm AA}$ Au+Au collisions at different energies $\sqrt{s_{\rm NN}} = 39,\ 62.4,\ 200$ GeV with U+U point added. Data show that U+U and Au+Au results with similar $N_{\rm part}$ are similar. However, the hot matter effects are expected to be the most significant in central collisions, therefore, the study of $N_{\rm part}$-dependence of J/ψ nuclear modification factor is important.

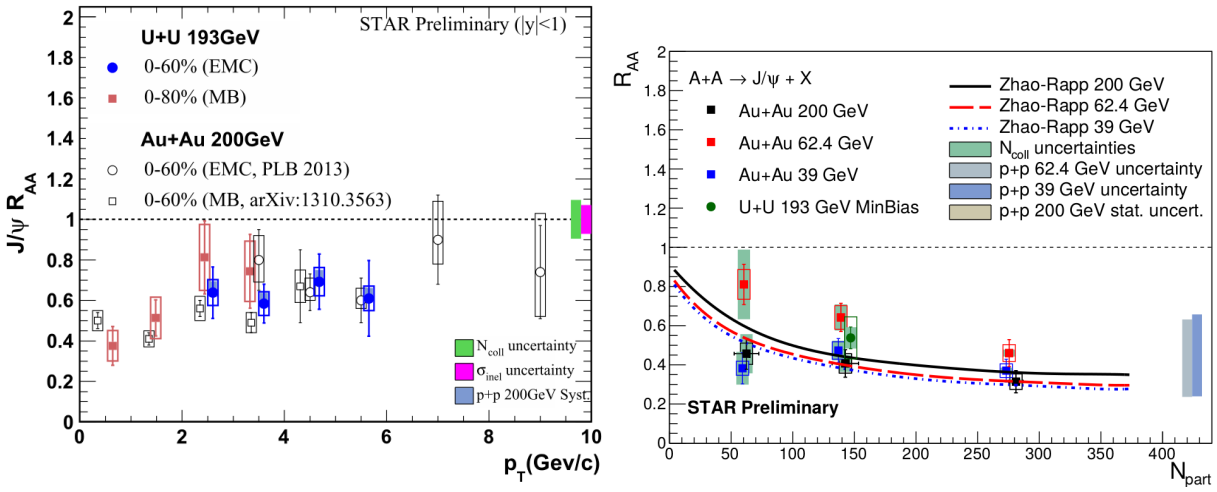

Figure 1.7: Left: J/ψ $R_{\rm AA}$ as a function of $p_{\rm T}$ in minimum-bias U+U collisions at mid-rapidity at $\sqrt{s_{\rm NN}} = 193$ GeV at STAR [17]. Right: $N_{\rm part}$ dependence of $R_{\rm AA}$ in Au+Au collisions at different energies, minimum bias U+U point included.

Chapter 2

The STAR experiment

The STAR (Solenoidal Tracker at RHIC) experiment [18] is a multi-purpose detector dedicated to study the strongly interacting matter at high temperature and high energy density. Its main purpose is detection, tracking and identification of charged particles at mid-rapidity.

STAR is located at the Relativistic Heavy Ion Collider (RHIC) in Brookhaven National Laboratory in New York, USA. RHIC is able to collide ions of different masses and at different energies. Moreover, RHIC is the only device in the world capable of colliding polarized protons. Until now collisions of p+p, p+Au, p+Al, d+Au, h+Au, Cu+Cu, Cu+Au, Au+Au and U+U at energies from 62.4 GeV to 500 GeV for protons and from 7.7 GeV to 200 GeV for heavy ions have been performed at RHIC [19].

Beams of accelerated ions in counter-rotating rings (blue and yellow) of RHIC and can be collided in six intersection points [20]. Currently, experiments STAR and PHENIX [21] are located at two of these points.

The massive 1200 tons weighting STAR detector located at 6 o'clock of RHIC shares its z-axis with the beam-line. It is cylindrical in shape and covers 2π in azimuth and two units of rapidity around the mid-rapidity.

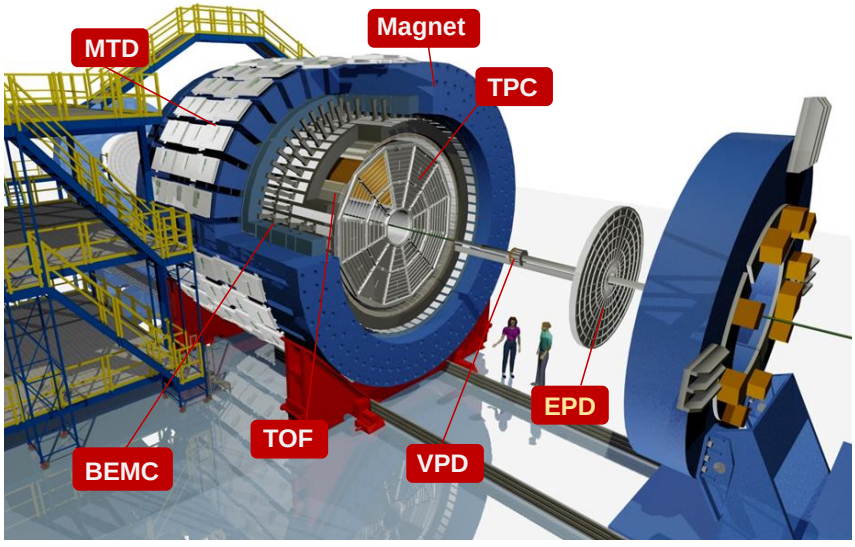

Figure 2.1: The layout of the STAR detector. Picture by Alex Schmah.

STAR consists of various subsystems, schematically shown in the Figure 2.1. These subsystems perform different tasks: they can be used for triggering, particle identification or tracking. Following sections are dedicated to detectors used in J/ψ analysis presented in this work. The Zero Degree Calorimeters together with the Time of Flight Detector performed the selection of

central events. The Time Projection Chamber, Time of Flight detector and Barrel Electromagnetic Calorimeter were used for identification of J/ψ daughter electrons.

2.1 Time Projection Chamber

The heart of the STAR detector, the Time Projection Chamber (TPC), is the main tracking device of STAR. It provides identification of charged particles according to their specific ionization energy loss in the material.

The layout of the TPC can be seen in the Figure 2.2. It is cylindrical in shape and surrounds the inner tracking system of the STAR detector located around the beam-pipe. TPC is 4.2 m long and has an inner diameter of the drift volume 1 m and outer diameter 4 m [22]. It covers pseudorapidity $|\eta| < 1.8$ and full azimuthal angle.

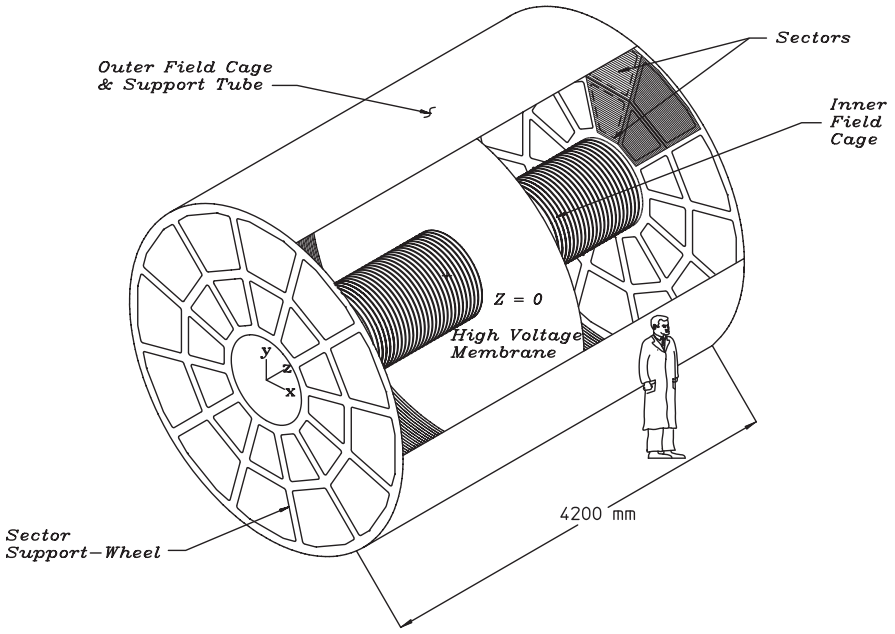

Figure 2.2: The Time Projection Chamber [22].

TPC sits in a uniform electric and magnetic field. The electric field of ca. 135 V/cm is generated by Central Membrane (cathode membrane) held at the voltage -28 kV and grounded anode end caps. The 0.5 T magnetic field is generated by the solenoidal STAR magnet [22].

TPC is filled with P10 gas (90% Argon, 10% Methane) operating at 2 mbar above the atmospheric pressure. In the operating electric field of TPC the drift velocity in the P10 gas is stable and insensitive to small variations in temperature and pressure and this is required.

TPC has anode read out system located on the end caps of the chamber consisting of 136 560 read-out modules based on Multi Wire Proportional Chambers technology [22]. Read-out pads are connected into pad rows and these are divided into 12 sectors. In each sector there are 13 inner and 32 outer pad rows. The inner sectors, located in the area of the highest track density, are equipped with smaller pads than the outer sectors to provide necessary better resolution.

2.1.1 Particle identification using TPC

As the primary ionizing particle emerging from collision traverses the volume of the TPC it ionizes the atoms of the gas. The electric field of the TPC causes that positive ions travel to the Central Membrane while the (secondary) electrons drift with a constant velocity $\approx$ 5.45 cm/μs [22] towards the end caps resulting in the drift time of $\lessapprox 40$ μs.

Since TPC has anode read-out system the path of the primary particle is reconstructed from the secondary electrons measured on pads on the end caps.

Magnetic field in which the TPC sits curves the trajectories of charged particles. Since the momentum of the particle is proportional to the radius of its curvature, tracking of the particles can determine their momenta. TPC enables to measure momenta over a range of 100 MeV/c to 30 GeV/c [23]. The relative momentum resolution of TPC was found to be $\sim$ 2% for the majority of the tracks [22]. It is improved as the number of hit points along the track increases and as the momentum of particle decreases.

As the primary particles ionize the atoms of the gas they loose the energy which turns out into the charge of secondary electrons collected in the TPC pads. The ionization energy loss of particle per unit of length dE/dx in a given medium (TPC gas) can be calculated for different particle species using the Bichsel functions [24] and compared with measured values. The relative resolution of energy loss in TPC was established to be 7% [25]. Figure 2.3 shows the measured and calculated energy loss of charged particles in the TPC as a function of the particle momentum. As can be seen from the figure, pions, kaons and protons can be well separated in the low p region (for $p < 1$ GeV/c). However, towards higher p_{T} energy loss bands of different particles overlap. In general, using the TPC, particles are identified over a momentum range from 100 MeV/c to $\sim$ 1 GeV/c. To extend particle identification capabilities towards higher p_{T} other detectors (e.g. TOF, BEMC) are needed.

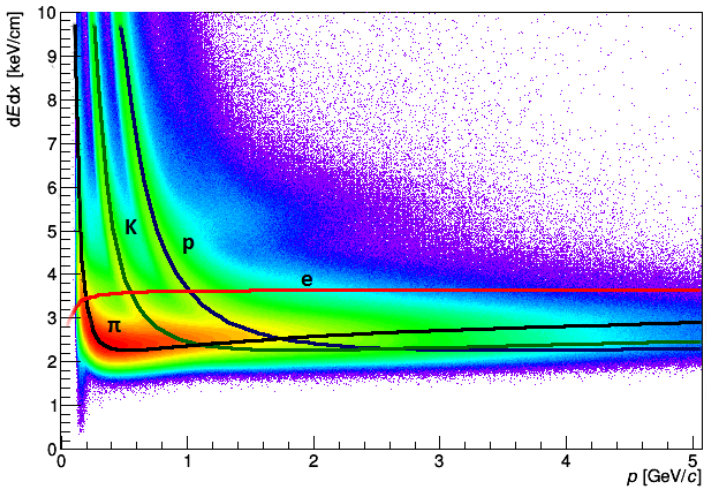

Figure 2.3: The energy loss of charged particles as a function of their momentum in 0-5% most central U+U collisions. Expected values for electrons e, pions π, kaons K and protons p obtained from Bichsel functions [24] are shown as colored curves.

2.2 Time of Flight Detector

The Time of Flight (TOF) detector extends the particle identification capabilities of the TPC. Moreover, it is also very important triggering device of the STAR detector. It is used to trigger on central collisions by requiring a high occupancy of hits on its modules.

TOF is in the shape of cylindrical shell around the TPC (see Figure 2.1) and covers the pseudorapidity $|\eta| < 0.9$ and full azimuthal angle.

TOF enables to measure the time of flight of the particle. In fact, TOF measures the "stop time" when the signal of the particle in any TOF detection pad is detected. In order to obtain the time of flight the information from STAR Vertex Position Detectors which measure the "start time" of the collision is used. Then, the time of flight is given as the difference between the stop time and start time. The TOF identification capabilities are often expressed in the words of the average value of the inverse velocity $1/\beta$ given as the ratio of the time of flight and the length s of associated track from the TPC.

Using the information from TPC about momentum p of the particle and its $1/\beta$, the mass m of the particle can be calculated according to:

$$m = \frac{p}{c}\sqrt{\left(\frac{1}{\beta}\right)^2 - 1}. \tag{2.1}$$

In the left panel of Figure 2.4 the momentum dependence of the mass resolution based on the TOF timing resolution 100 ps for protons, kaons, pions and deuterons is illustrated [26]. The right panel of Figure 2.4 shows measured $1/\beta$ as a function of particle momentum for electrons, pions, kaons, protons and deuterons. The theoretical curves are obtained using the particle masses [27] and Equation 2.1.

Together with the TPC the TOF can improve the identification of low momentum particles. It is effective in separation of electrons from heavier hadrons at low momenta to ~ 1.4 GeV/c, pions and (anti)protons are identified for p up to 7 - 8 GeV/c, kaons to ~ 3 GeV/c and electrons from 150 MeV/c to 4 GeV/c [28]. However, as can be seen from the Figure 2.4 towards the intermediate momenta the capabilities of TOF are not sufficient for particle identification – the mass bands and $1/\beta$ of different particle species overlap. For this reason information from Barrel Electromagnetic Calorimeter has to be used at higher momenta.

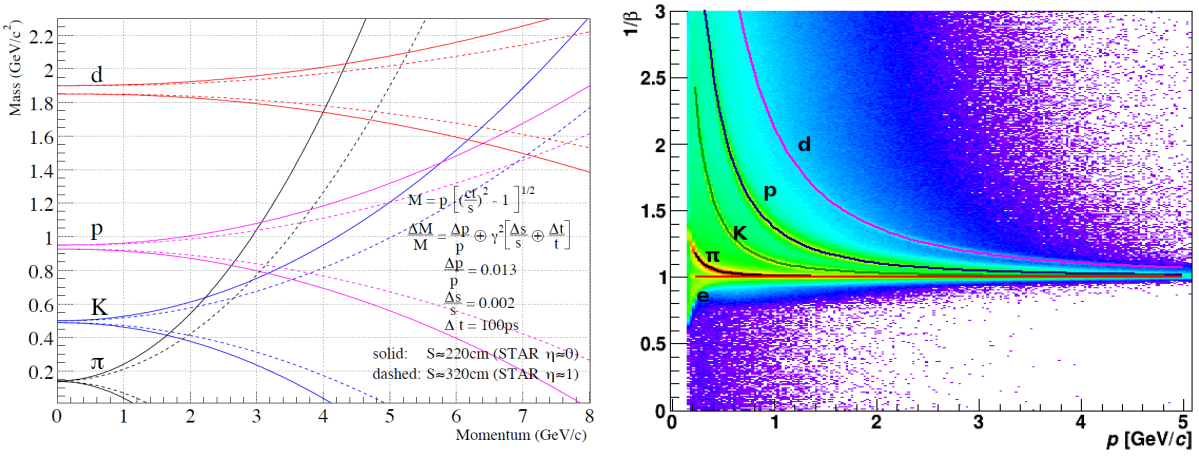

Figure 2.4: Left: The momentum dependence of the mass resolution for the total TOF resolution 100 ps for protons, kaons, pions and deuterons [26]. Right:$1/\beta$ of charged particles as a function of their momentum in 0-5% most central U+U collisions. Calculated values for electrons e, pions π, kaons K, protons p and deuterons d according to 2.1 are shown as colored curves.

2.3 Barrel Electromagnetic Calorimeter

The Barrel Electromagnetic Calorimeter (BEMC) measures energy of electromagnetic showers produced by high momentum particles. It is also used to trigger on events with a large deposit of energy of a jet or high p_{T} particle in BEMC towers (brifly described later)(HT trigger).

BEMC is barrel of diameter ca. 4.4 m. It is located between the TOF detector and the STAR magnet. It covers pseudorapidity $|\eta| < 1$ and full azimuthal angle ϕ. It consists of 120 calorimeter modules of the size $\Delta\eta \times \Delta\phi \simeq 1 \times 0.1$, each of each of which is segmented into 40 towers, 2 in ϕ and 20 in η, with each tower being 0.05 in $\Delta\phi$ by 0.05 in $\Delta\eta$. The schematic drawing of the BEMC module is illustrated in the Figure 2.5. Each module consists of a lead-scintillator stack and Barrel Shower Maximum Detectors (BSMD) [29]. As high energy particles pass the layers of lead and scintillator. Lead plates are absorbers in which the particles lose energy and as a result the electromagnetic showers develop. while the role of the scintillator layers is to transform the energy of particles from shower to energy of photons and to sample this energy.

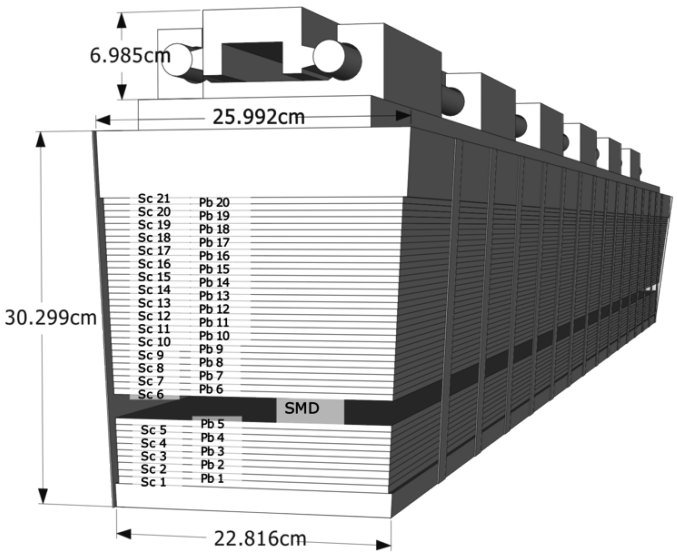

Figure 2.5: Schematic drawing of the BEMC module [30].

Since BEMC has a total radiation length $\sim$ 20 X_0 [29] electrons are expected to deposit their whole energy in the calorimeter while hadrons do not. Therefore, for high momentum electrons energy-to-momentum ratio E/pc (where E is energy deposited in the BEMC towers and p is momentum from TPC) is ~ 1 while for hadrons it is less than 1. So, at high momentum the BEMC towers provide electron-hadron separation via E/pc.

2.4 Zero Degree Calorimeter

Triggering system of the STAR detector is a complicated system consisting of different levels of logic. In this system the signals from the fast detectors (Vertex Position Detectors, Zero Degree Calorimeters, Beam Beam Counters, or already mentioned TOF and BEMC) are processed in bunch crossing rate 1 MHz [31] and decisions which events should be recorded and whether to "switch on" read-out of slow detectors (required primarily for tracking and particle identification, e.g. TPC) are made.

Central collisions analyzed in this work were selected using the ZDC+TOF triggers. Since

TOF detector has been already described we turn our attention to the two Zero Degree Calorimeters (ZDCs). They are situated at 18.25 m from the intersection point outside of the RHIC magnets as illustrated in Figure 2.6. Each ZDC assembly consists of three modules. Each module consists of a series of tungsten plates alternating with layers of wavelength shifting fibers that route Čerenkov light to a photo-multiplier tube. By detecting the Čerenkov radiation the ZDCs measure the number of spectator neutrons from collisions.

ZDCs are used for triggering on central collisions and for beam monitoring [32, 5].

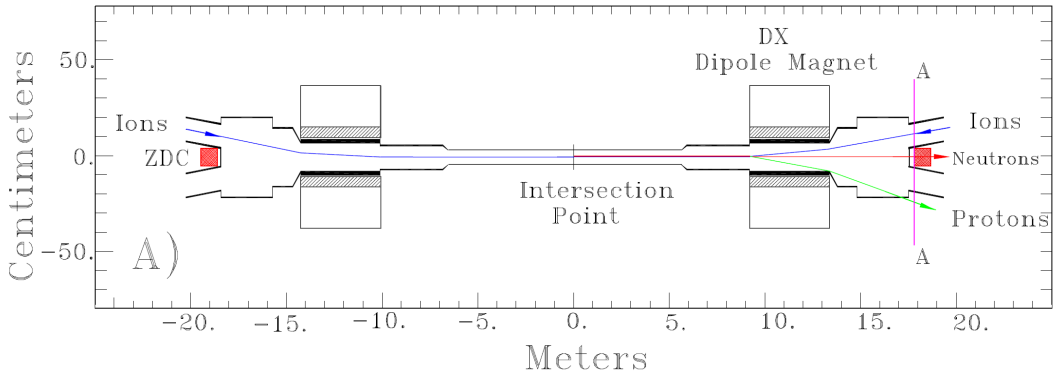

Figure 2.6: Plan view of the collision region with the location of ZDC detectors illustrated. Deflection of charged fragments and protons is indicated [32].

Chapter 3

Data analysis

This chapter focuses on the data analysis leading to the extraction of raw J/ψ signal in 0-5% most central U+U collisions at the STAR experiment. J/ψ was reconstructed via the electron-positron decay channel $J/\psi \rightarrow e^+e^-$ with branching ratio B.R. = (5.971 $\pm$ 0.032) % [27]). The method of J/ψ signal extraction is described as a sequence of different criteria applied on analyzed events, tracks and J/ψ daughter electron (positron) candidates.

3.1 Data and triggers

In this analysis the data taken from U+U collisions recorded at RHIC at the center-of-mass energy $\sqrt{s_{\rm NN}} = 193$ GeV in Run 12 in year 2012 were used. Since the aim of the analysis was to study the J/ψ in central U+U collisions, only the events satisfying the 0-5% centrality triggers, namely those labeled central-5 and central-5-protected, were analyzed.

The labeling "central-5" denotes the centrality class of events which are the subject to selection. In general, the 0-5 % centrality triggers select the events by requiring a small signal deposited in the ZDC detectors as well as a large multiplicity from the barrel TOF.

Attribute "protected" means that there is an algorithm that looks at the past and future history of information in the trigger detectors (BBC hits, ZDC energy, TOF hits) to reduce (but not able to completely remove) additional occupancy in the TPC caused by pile-up of other events in the 40 μs readout time.

Using the central triggers ca. 115 M events were selected and these were used for further studies. Figure 3.1 shows the multiplicity distribution of events used in this analysis.

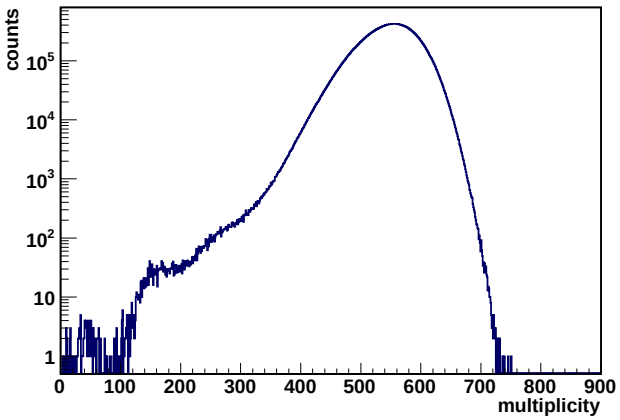

Figure 3.1: Multiplicity distribution of 0-5% most central events according to TOF+ZDC central triggers.

3.2 Event selection

In further analysis only those events for which the longitudinal distance (i.e. the distance in the direction of the z-axis) between the z-coordinate of their primary vertex reconstructed as an intersection point of the TPC tracks ${v_Z}^{\mathrm{TPC}}$ and the center of the detector (${v_Z}^{\mathrm{TPC}}$) was lower than 30 cm were selected (shown in the left panel of Figure 3.2). This requirement was used to ensure that the efficiency of reconstruction will not depend on v_Z. Thus, only collisions in the center of the detector were analyzed.

The primary vertex can be determined also by the Vertex Position Detectors (VPD). To remove the pile-ups only the events for which $|v_Z^{\mathrm{TPC}} - v_Z^{\mathrm{VPD}}| <$ 3 cm (see right panel of Figure 3.2) were analyzed. Applying the event cuts the number of analyzed events was reduced to $\sim$ 56 M.

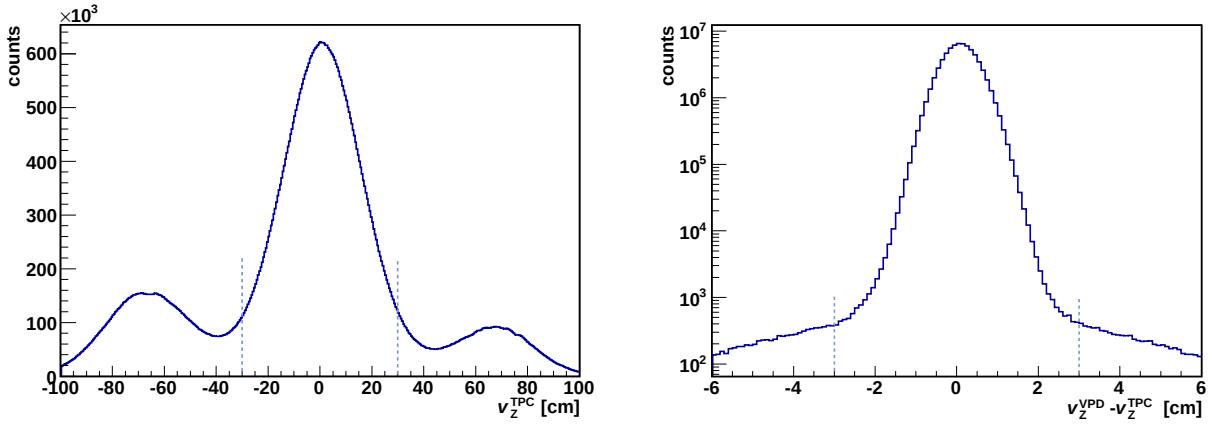

Figure 3.2: Left: ${v_Z}^{\mathrm{TPC}}$ distribution of analyzed events before the v_Z^{TPC} cut. Dashed lines denote the applied cut. Right: $v_Z^{\mathrm{TPC}} - v_Z^{\mathrm{VPD}}$ distribution of analyzed events after v_Z^{TPC} cut. Dashed lines denote the $v_Z^{\mathrm{TPC}} - v_Z^{\mathrm{VPD}}$ cut.

3.3 Track selection

In the analyzed events J/ψ daughter electrons (positrons) were selected from the so-called primary tracks.

In addition to global tracks which are obtained from fitting the hits in the TPC, the primary tracks are reconstructed by refitting the hits in the TPC taking also the collision vertex into account as a fit point. In other words we require the track to originate in (or very close to) the primary vertex. This requirement comes from the very short lifetime of J/ψ which is $\approx 7.10^{-20}$ s [27] so J/ψ is not expected to travel far from the primary vertex before it decays into e.g. daughter electrons. Hence, the primary tracks are considered to perform good description of J/ψ daughter electrons (positrons).

3.3.1 Track quality requirements

In this analysis the primary tracks were selected according to the following quality requirements:

- The distance of the closest approach (DCA) of the track to the primary vertex of the event had to be less than 3 cm.
- Particle trajectories are reconstructed by fitting the hits on the TPC pads. To ensure good quality of reconstructed tracks the minimum number of reconstructed hits in TPC

was required to be 20.
- The ratio of fitted hits to all possible hits (maximum number of hit points) on the TPC pads had to be larger than 0.51. This requirement was used to remove split tracks (misidentified as different tracks) which decrease the considered ratio.

3.3.2 Kinematic requirements - p_{T} cut

Following kinematic requirements on electron candidates were also used:

- Only tracks with pseudorapidity $\eta < 1.0$ were accepted. This requirement is based on the acceptance of the TPC.
- We required the p_{T} of the primary tracks to be above 0.2 GeV/c in order to reach the outer radius of the TPC.
- In addition to the previously mentioned requirements on primary tracks only the electrons (positrons) with transverse momenta above 1.0 GeV/c were accepted for the analysis of J/ψ signal. The p_{T} cut was motivated by the shape of the p_{T} distribution of J/ψ daughter electrons obtained from simulation. There is only a small fraction of J/ψ decays into electrons (positrons) with p_{T} below $\sim$ 0.8 GeV/c. For the analysis of photonic electrons used for efficiency calculations this p_{T} cut was not used.

3.4 Electron identification

From the primary tracks satisfying criteria described above J/ψ daughter electron (positron) candidates were selected. The electron (positron) candidates had to fulfill cuts on TPC, TOF and BEMC signal described in following sections.

3.4.1 TPC cut

The electron (positron) data sample was selected using only those tracks for which their dE/dx fluctuates around the corresponding theoretical value dE/dx_{Bichsel} [24] shown in Figure 2.3. This method of selection is connected with the variable $n\sigma_{\mathrm{e}}$ which gives dE/dx normalized to dE/dx_{Bichsel} for electrons in the logarithm and scaled by the dE/dx resolution $\sigma_{dE/dx}$:

$$n\sigma_{\mathrm{e}} = ln\left(\frac{dE/dx}{dE/dx_{\mathrm{Bichsel}}}\right)/\sigma_{dE/dx} \tag{3.1}$$

In the J/ψ analysis $n\sigma_{\mathrm{e}}$ was required to be in the range between -1.5 and 2.0. The asymmetric cut was applied in order to decrease the contamination from pions at negative $n\sigma_{\mathrm{e}}$ which can be seen in the left panel of Figure 3.3. TPC $n\sigma_{\mathrm{e}}$ cut was required for all electron (positron) candidates.

3.4.2 TOF cut

For low momentum particles $1/\beta$ measured by TOF is ~ 1 for electrons while it is > 1 for hadrons. Towards higher momenta ($p > 1.4$ GeV/c) $1/\beta$ of e, π, p, K, d approaches to 1 and it is not possible to select the electrons only with the TOF detector. In our analysis the TOF cut was applied as follows: if $p < 1.4$ GeV/c we required electron candidates to have a valid TOF signal, i.e. we required TOFMatchFlag > 0 and $|y_{\mathrm{local}}| < 1.8$ cm where y_{local} is distance of the track projection and the center of TOF pad and $1/\beta$ to be in the range from 0.970 to 1.025. For particles with momenta higher than 1.4 GeV/c TOF was used as veto. Particle was accepted if it did not have the signal in TOF. On the other hand, if particle had a good signal in TOF but $1/\beta$ was not in the required range it was not accepted. Right panel of Figure 3.3 shows $1/\beta$ of

tracks which satisfy primary track quality requirements, TPC and BEMC cut. The lines on the plot illustrate the TOF cut.

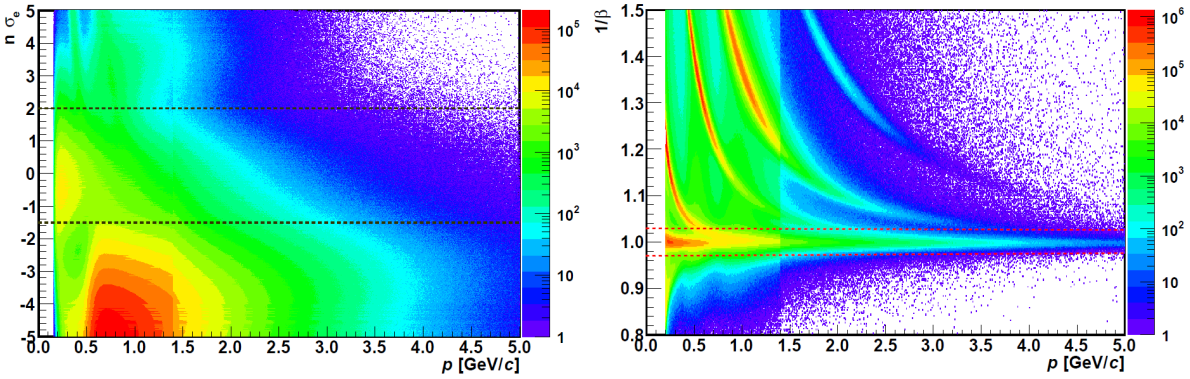

Figure 3.3: Left: $n\sigma_{\mathrm{e}}$ of tracks satisfying primary track quality requirements, TOF and BEMC cuts. Black dashed lines denote the $n\sigma_{\mathrm{e}}$ cut. Right: $1/\beta$ of particles which satisfy TPC and BEMC cuts. Red dashed lines on the plot illustrate the TOF cut.

3.4.3 BEMC cut

To identify particles of momenta higher than 1.4GeV/c the BEMC is needed. BEMC can distinguish between electrons and hadrons with higher momenta according to the ratio pc/E (E is deposited energy in the BEMC tower, p is the momentum of the particle required by TPC) which should be ~ 1 for electrons and > 1 for hadrons. However, different effects (leakage/gain of the energy to/from neighboring towers) modify this ratio. Thus the electron candidates were required to deposit energy $E > 0.15$ GeV in the highest energy BEMC tower and satisfy the criterion: $0.7 < pc/E < 2.0$.

3.5 Raw J/ψ yield

J/ψ signal was reconstructed from the decay of J/ψ mesons into e^-e^+ pairs. To find the J/ψ signal each electron candidate was combined with each positron candidate satisfying electron cuts described in previous sections. The invariant mass of electron-positron pairs was calculated according to the formula

$$M_{\mathrm{inv}} = \sqrt{2p_1p_2(1-\cos\alpha)} \tag{3.2}$$

where p_1 and p_2 are momenta of electron(positron) candidates and α is the angle between p_1 and p_2. We used cut on J/ψ rapidity: $-1 < y < 1$ to analyze the signal only at mid-rapidity.

However, the created e^-e^+ pairs contain not only the pairs coming from J/ψ decay but also randomly paired e^-e^+. These represent significant combinatorial background needed to be subtracted. Two methods of combinatorial background estimation were used in this analysis:

- **Like-sign background** - the like-sign pairs (e^-e^- and e^+e^+) were combined within the same events and invariant mass of these pairs was calculated.
- **Mixed event background** - we combined electrons and positrons from different events with similar event conditions which were multiplicity and primary vertex position. Events were divided into 10 multiplicity and 20 v_{Z} bins. For each multiplicity and v_{Z} bin the combinatorial background was calculated combining each e^+ from one event with each e^- from the other event always at least 10 events were mixed. Mixed event background was then normalized to the like-sign background in the invariant mass region (2.0, 3.6) GeV/c^2

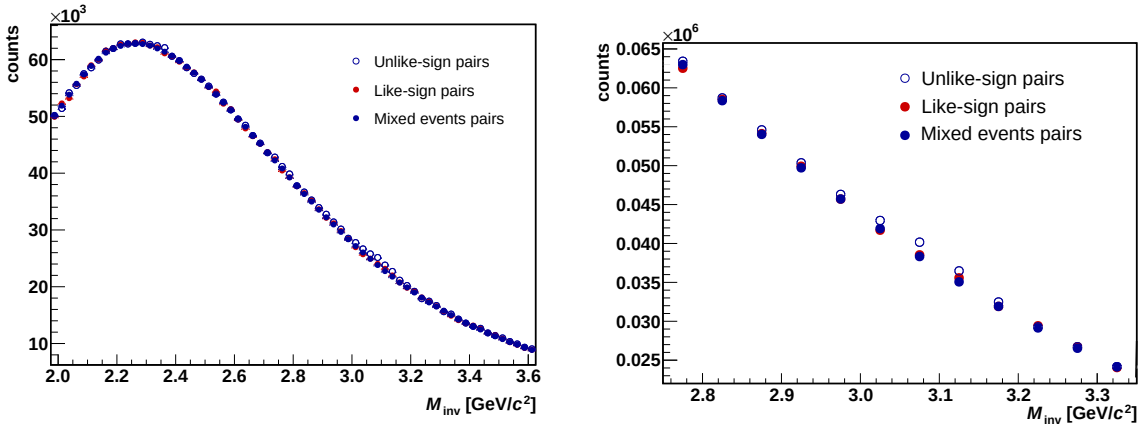

Figure 3.4: Left: The invariant mass spectra of e^+e^- unlike-sign pairs, mixed events pairs and like-sign pairs in 0-5 % most central U+U collisions. Right: Zoom on the region around J/ψ mass peak.

around J/ψ invariant mass peak. This method of combinatorial background subtraction enables us to increase the statistics (decrease the statistical error of the background) compared with like-sign method.

Both methods of combinatorial background subtraction were tested in studied J/ψ p_{T} bins. Figure 3.4 shows the invariant mass spectra of e^-e^+ unlike-sign pairs, mixed events pairs and e^-e^-, e^+e^+ like-sign pairs used in the J/ψ signal studies in 0-5% most central U+U collisions for J/ψ p_{T} integrated. As can be seen, there is a visible peak in the region around J/ψ invariant mass.

Due to its advantage mentioned above only the mixed event background was used for the description of the combinatorial background for the rest of the analysis. However, even after the subtraction of the combinatorial background the so called residual background still remains. Therefore the invariant mass shape was fitted with the Crystal ball function [33] to describe the signal shape and the linear function (in notation used here with the constant term P_0 and slope P_1) to describe the residual background. Other functions such as second and third degree polynomials and exponential function were also used for residual background fitting (as illustrated in Figure 5.1). However, the best agreement with data was achieved with the linear function. The Crystal ball function is similar to a Gaussian function but it has a power-low tail which is used to describe the asymmetry of the peak. This can be caused by the bremsstrahlung of J/ψ daughter electrons (positrons) which are reconstructed with lower invariant mass. The Crystal ball function can be expressed as [33]:

$$f_{CB}(m) = \begin{cases} \frac{N}{\sqrt{2\pi}\sigma} \exp\left(-\frac{(m-m_0)^2}{2\sigma^2}\right), & \text{for } \frac{m-m_0}{\sigma} > -\alpha; \\ \frac{N}{\sqrt{2\pi}\sigma}\left(\frac{n}{|\alpha|}\right)^n \exp\left(-\frac{|\alpha|^2}{2}\right)\left(\frac{n}{|\alpha|} - |\alpha| - \frac{m-m_0}{\sigma}\right)^{-n}, & \text{for } \frac{m-m_0}{\sigma} \leq -\alpha. \end{cases} \tag{3.3}$$

N is the normalization constant, m_0 is common mean (in this case J/ψ invariant mass), σ is variance, α defines the transition between the Gaussian and the power-law functions and n describes an exponent of the power law tail [33].

Figure 3.5 shows the J/ψ invariant mass peaks and fitting functions for three J/ψ p_{T} bins: 0 - 1 GeV/c, 1 - 3 GeV/c, 3 - 7 GeV/c and for J/ψ p_{T} integrated in 0-5 % most central U+U collisions. While at lower transverse momenta clear J/ψ peak can be observed for p_{T} = 3 - 7 GeV/c the signal peak is small. In general, the data points have large statistical errors, significant fluctuations of the residual are observed and this affects the quality of the fit. The fitting of the peak serves mainly to estimate the residual background.

Raw J/ψ yield was calculated by the bin counting in the invariant mass region (2.9-3.2) GeV/c^2 after subtracting the residual background obtained from the fit. This range was used in order to include substantial part of the yield smeared towards lower invariant mass.

Significance s of the J/ψ signal can be calculated as

$$s = \frac{S}{\sqrt{S+B}} = \frac{S}{\sigma_S} \tag{3.4}$$

where S is the number of J/ψs in given invariant mass range, σ_S its error and B is the background (combinatorial+residual) in the same region.

Table 3.1 shows an overview of J/ψ raw yields in different J/ψ p_T bins and for J/ψ p_T integrated, its error and corresponding significance. J/ψ raw yield error was calculated as the error of the bin counting combined with the integral error of residual background.

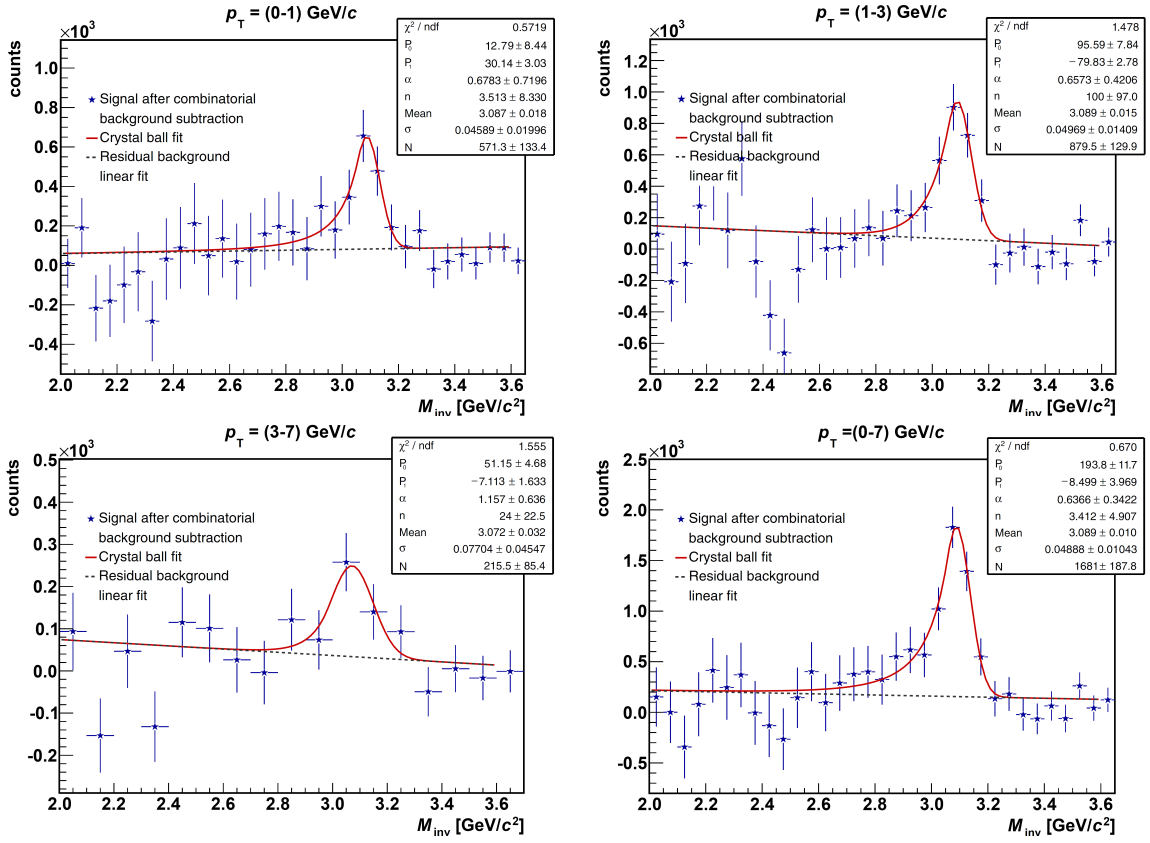

Figure 3.5: J/ψ signal after combinatorial background subtraction for for J/ψ p_T 0 - 1 GeV/c, 1 - 3 GeV/c, 3 - 7 GeV/c and for J/ψ p_T 0 - 7 GeV/c integrated. Signal is fitted with the Crystal Ball function, residual background with the linear function.

p_T [GeV/c]	Raw yield	Error	Significance
0–1	1660	370	4.5
1–3	2750	400	6.8
3–7	450	140	3.2
0–7	4790	560	8.6

Table 3.1: Raw yield, error of the raw yield and significance of the J/ψ signal for different J/ψ p_T bins.

Chapter 4

Signal corrections

By setting the requirements on electron (positron) signal in TPC, TOF and BEMC and the cut on J/ψ invariant mass window only a fraction of J/ψ produced in central U+U collisions is reconstructed. Therefore, to calculate the J/ψ invariant yield in central U+U collisions the correction of J/ψ raw yield on the number of J/ψ which did not fulfill the different signal requirements is needed. In this chapter J/ψ signal corrections are described and quantified by corresponding acceptance and efficiency factors.

4.1 J/ψ reconstruction efficiency

J/ψ reconstruction efficiency ϵ_{reco} quantifies the estimated fraction of J/ψ raw yield reconstructed in this analysis out of the number of J/ψ produced in studied U+U collisions. ϵ_{reco} can be expressed as function of J/ψ p_{T} by the formula:

$$\epsilon_{\text{reco}}(p_{\text{T}}) = \epsilon_{\text{folded}}(p_{\text{T}}) \times \epsilon_{\text{count}}(p_{\text{T}}) \tag{4.1}$$

where given terms denote contributions to signal corrections: J/ψ folded reconstruction efficiency ϵ_{folded} and signal counting correction ϵ_{count} which includes correction on the number of J/ψ reconstructed outside the range of the J/ψ invariant mass cut and the correction on bremsstrahlung of electrons (positrons).

J/ψ folded reconstruction efficiency can be further expressed as:

$$\epsilon_{\text{folded}}(p_{\text{T}}) = \epsilon_{\text{geom} \times \text{acc}}(p_{\text{T}}) \times \sum_{p_1,p_2} \epsilon_{\text{e}^-}(p_1) \times \epsilon_{\text{e}^+}(p_2) \times \omega(p_{\text{T}}, p_1, p_2) \tag{4.2}$$

where $\epsilon_{\text{geom} \times \text{acc}}$ is the J/ψ TPC tracking efficiency and geometrical acceptance, and ϵ_{e^-} (ϵ_{e^+}) is the efficiency of J/ψ decay electron (positron) identification and $\omega(p_{\text{T}}, p_1, p_2)$ is the weighting factor. $\omega(p_{\text{T}}, p_1, p_2)$ denotes the ratio of J/ψs with transverse momenta in given p_{T} bin with daughter electrons and positrons with momenta in bins p_1 and p_2 to all of J/ψ. $\omega(p_{\text{T}}, p_1, p_2)$ was estimated from the simulation which is described in following section. It was not estimated from data since J/ψ were analyzed using the requirement $p_{\text{T}} > 1.0$ GeV/c on daughter electrons (positrons) which was included in calculation of $\epsilon_{\text{geom} \times \text{acc}}$ (it could not be counted twice).

All the contributions to J/ψ reconstruction efficiency mentioned above are described in more detail in following sections.

4.1.1 TPC tracking efficiency and geometrical acceptance

TPC tracking efficiency and geometrical acceptance was determined from simulation. Monte Carlo simulated J/ψ were embedded into real events and the interaction of daughter electrons

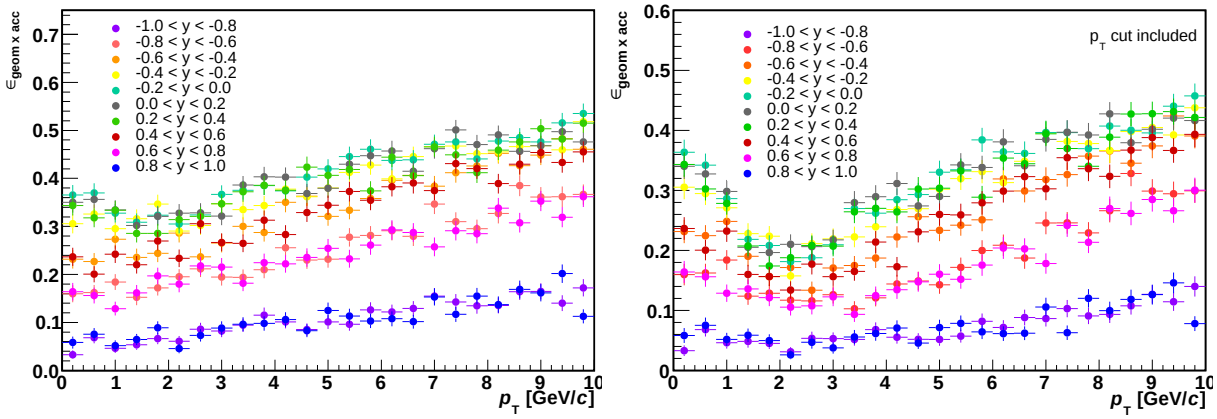

Figure 4.1: TPC tracking efficiency $\epsilon_{\text{geom}\times\text{acc}}$ as a function of J/ψ p_{T} in different rapidity bins before (left) and after (right) p_{T} cut on daughter electrons.

(positrons) with detector material was studied using the GEANT simulation. Then the same TPC track quality and acceptance requirements were used on simulated sample as on real tracks.

Since the embedding for J/ψ in central U+U collisions was not produced at the time when this work was finalized, temporarily, the embedding for J/ψ in Run 11 0-5 % most central Au+Au collisions at 200 GeV was used in the analysis.

In order to shorten the computing time, p_{T} and rapidity spectra of simulated J/ψ were produced as flat. To make the shape of these distributions more realistic the p_{T} spectrum was weighted by experimentally obtained function [34]

$$\frac{dN}{dp_{\text{T}}} = \frac{A}{(1+(p_{\text{T}}/b)^2)^n}. \tag{4.3}$$

This shape was used for the description of J/ψ p_{T} spectrum in 200 GeV p+p collisions at PHENIX [34]. A is normalization factor, b and n are parameters from [34]. In addition, J/ψ y spectrum was weighted with the analyzed J/ψ y distribution from real data.

As mentioned above the simulated electron (positron) daughters of the embedded J/ψ that were accepted by the TPC geometry were reconstructed using the same track quality requirements as the real data. TPC tracking efficiency and geometrical acceptance was then calculated as the ratio of the number of reconstructed embedded J/ψ to the number of Monte Carlo simulated J/ψ. Two panels of Figure 4.1 show the TPC tracking efficiency as a function of J/ψ p_{T} in different rapidity bins. To illustrate the effect of $p_{\text{T}} > 1$ GeV/c cut applied on daughter electrons (positrons) the left panel of Figure 4.1 shows $\epsilon_{\text{geom}\times\text{acc}}$ before the p_{T} cut applied while the right panel shows $\epsilon_{\text{geom}\times\text{acc}}$ with the p_{T} cut included. As can be seen p_{T} cut systematically decreased $\epsilon_{\text{geom}\times\text{acc}}$. The effect is the most significant for J/ψ with $p_{\text{T}} \approx 1-3$ GeV/c and $-0.4 < y < 0.4$.

4.1.2 Single electron identification efficiency

The efficiency of single electron identification covers detector cut efficiency − since different cuts on TPC, TOF and BEMC signal were used only some fraction of electrons was accepted − and matching efficiency − which represents probability that the track leaves signal in the detector (TOF or BEMC).

Resulting efficiency of single electron identification ϵ_{e} includes all mentioned efficiencies and can be expressed as

$$\epsilon_{\mathrm{e}} = \begin{cases} \epsilon_{\mathrm{TPCcut}} \times \epsilon_{\mathrm{TOFcut}} \times \epsilon_{\mathrm{TOFmatch}} & \\ & \text{for } p \leq 1.4\mathrm{GeV}/c; \\ \epsilon_{\mathrm{TPCcut}} \times [\epsilon_{\mathrm{TOFcut}} \times \epsilon_{\mathrm{TOFmatch}} + (1 - \epsilon_{\mathrm{TOFmatch}})] \times \epsilon_{\mathrm{BEMCcut}} \times \epsilon_{\mathrm{BEMCmatch}} & \\ & \text{for } p > 1.4\mathrm{GeV}/c. \end{cases} \quad (4.4)$$

In order to calculate single electron identification efficiency from data we need to select pure electron data sample without hadron contamination (in an ideal case). For this purpose pairs of photonic electrons (which come from γ conversions, π^0 and η decays) with low invariant mass $m_{\mathrm{inv}} < 12.5$ MeV/c^2 are selected. The photonic electron candidates are required to satisfy all track quality and kinematic cuts (as summarized in Table **??**). Moreover, all electron identification cuts, i.e. TPC, TOF and BEMC cuts, are applied on the first photonic electron candidate from the pair while the second one, not biased by the studied detector, is used for efficiency studies. Since the probability that electron has a signal in TOF and BEMC is correlated signal in TOF was required for the photo-candidate in BEMC matching efficiency calculation. In order to remove non-photonic contributions from the studied sample, the like-sign background photonic electron pairs were subtracted from the unlike-sign pairs and the photonic electrons from subtracted sample were studied.

TPC cut efficiency

TPC cut efficiency $\epsilon_{\mathrm{TPCcut}}$ estimates the fraction of photonic electron candidates satisfying the $n\sigma_{\mathrm{e}}$ cut used in the analysis, $-1.5 < n\sigma_{\mathrm{e}} < 2.0$. The $n\sigma_{\mathrm{e}}$ distributions of photonic electrons were fitted with Gaussian function in each momentum bin in the range $-2.0 < n\sigma_{\mathrm{e}} < 3.0$ (this range was chosen due to the residual contamination from other particles, mostly pions). Left panel of Figure 4.2 shows the $n\sigma_{\mathrm{e}}$ distribution of electrons in the momentum range $(0.4 - 0.6)$ GeV/c with Gaussian fit applied.

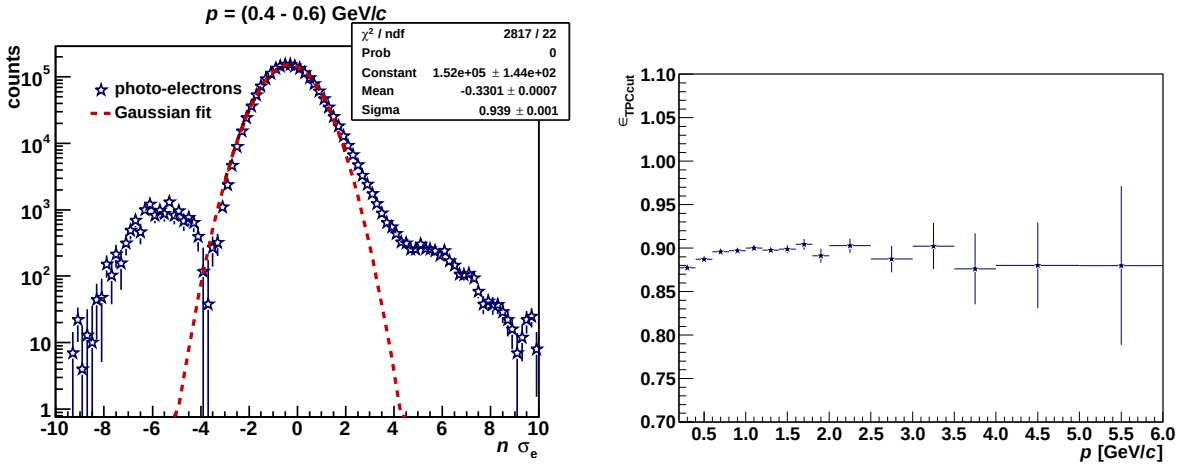

Figure 4.2: Left: $n\sigma_{\mathrm{e}}$ distribution for photonic electrons with momenta $(0.4 - 0.6)$ GeV/c. Right: TPC cut efficiency $\epsilon_{\mathrm{TPCcut}}$ given as a function of photonic electron momentum p.

The TPC cut efficiency was then calculated as the ratio of the area under the Gaussian curve in the cut range $-1.5 < n\sigma_{\mathrm{e}} < 2.0$ and the area under the Gaussian curve in its whole range. Resulting TPC cut efficiency given as a function of photonic electron momentum can be seen in the right panel of Figure 4.2. To remove the y-dependence of TPC cut efficiency, TPC cut efficiency was weighted by the rapidity distribution of J/ψ in studied momentum bins and so included in further calculations.

TOF cut efficiency

The TOF cut efficiency was calculated as the ratio of the number of photonic electron candidates satisfying $1/\beta$ cut used in the analysis, $0.970 < 1/\beta < 1.025$, to the number of photonic electron candidates satisfying wider cut, $0.93 < 1/\beta < 1.07$, which should be wide enough to cover all the electron candidates. Left panel of Figure 4.3 shows $1/\beta$ distribution of photonic electron candidates in momentum bin $(0.4 - 0.6)$ GeV/c. Resulting TOF cut efficiency as a function of electron momentum is shown in the right panel of Figure 4.3. As can be seen, the TOF cut efficiency shows constant trend as a function of momentum and is almost 99% what indicates that the $1/\beta$ cut used in the analysis is wide enough to cover practically all electrons (positrons).

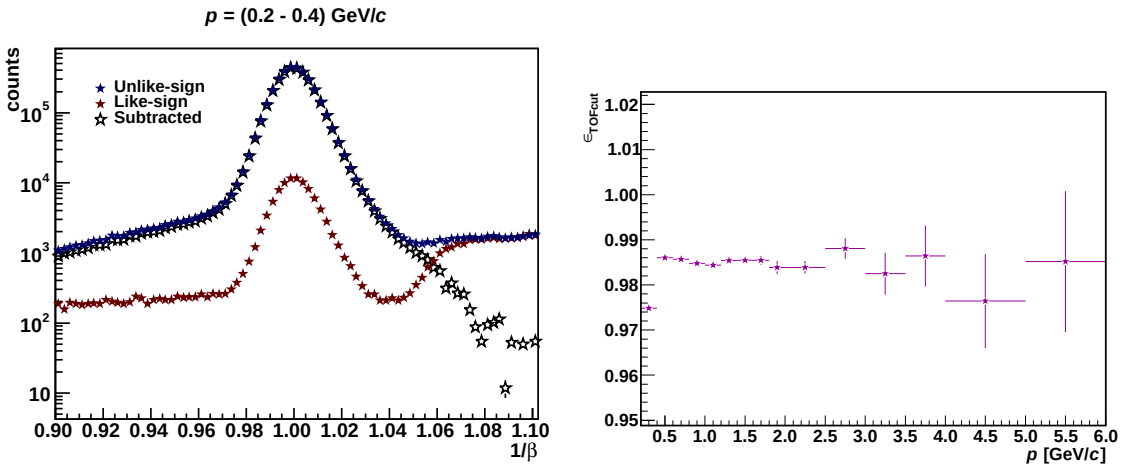

Figure 4.3: Left: $1/\beta$ of photonic electron candidates with momenta $(0.4 - 0.6)$ GeV/c. Right: TOF cut efficiency ϵ_{TOFcut} as a function of photonic electron momentum p.

TOF matching efficiency

TOF matching efficiency was calculated as the ratio of the number of photonic electron candidates with valid TOF signal to all photonic electron candidates. Left panel of Figure 4.5 shows resulting TOF matching efficiency as a function of electron momentum.

BEMC cut efficiency

The BEMC cut efficiency was calculated as the ratio of photonic electrons candidates satisfying the BEMC cut $0.7 < pc/E < 2.0$ (in terms of E/pc: $0.5 < E/pc \lesssim 1.43$) to those with pc/E in the wider range, $0.0 < pc/E < 5.0$, which should be wide enough to cover all photonic electron candidates.

Left panel of Figure 4.4 shows E/pc of photonic electron candidates in one momentum bin $(1.8 < p < 2.0$ GeV/$c)$. Unlike-sign photonic electron candidates, like-sign background and subtracted data sample are shown. Resulting BEMC cut efficiency as a function of electron momentum is in the right panel of Figure 4.4.

BEMC matching efficiency

Similarly to the TOF matching efficiency, the BEMC matching efficiency was calculated as the ratio of the number of photonic electron candidates with valid BEMC signal and all photonic electron candidates. Here the valid BEMC signal means that there is a hit recorded in the BEMC

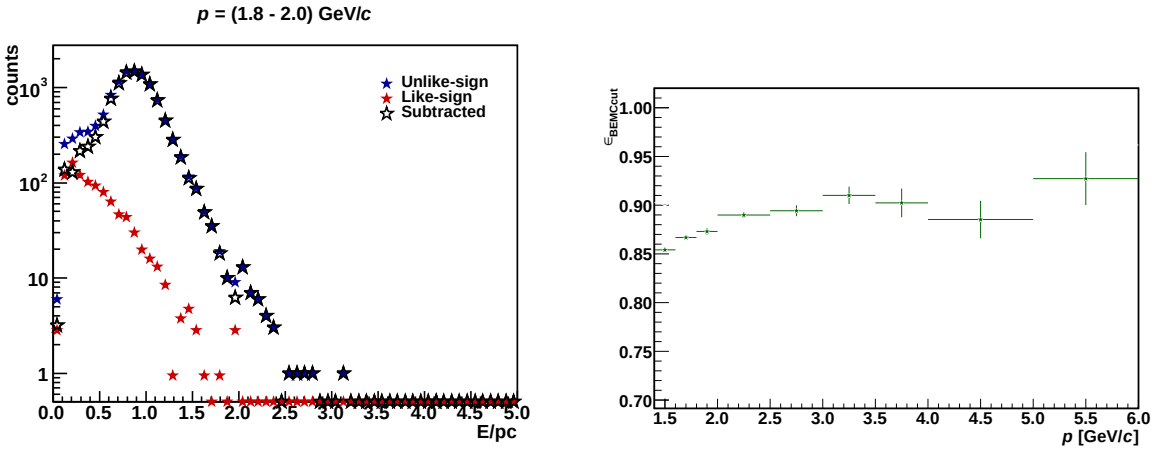

Figure 4.4: Left: pc/E distribution of photonic electron candidates in the momentum bin $1.8 < p < 2.0$ GeV/c. Right: BEMC cut efficiency $\epsilon_{\mathrm{BEMCcut}}$ as a function of electron momentum p.

tower to which the track from TPC projects. Right panel of Figure 4.5 shows resulting BEMC matching efficiency as a function of photonic electron momentum.

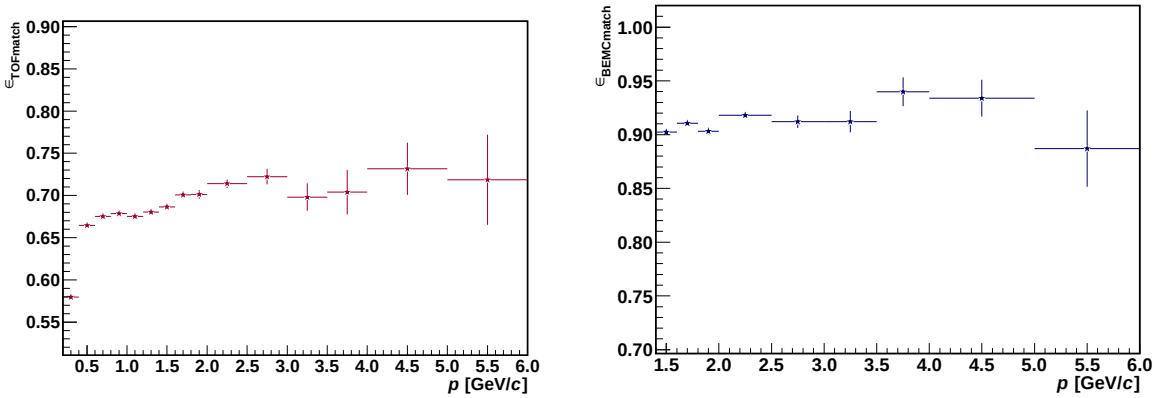

Figure 4.5: TOF (left) and BEMC (right) matching efficiency $\epsilon_{BEMCmatch}$ as a function of photonic electron momentum p.

Resulting single electron identification efficiency

Left panel of Figure 4.6 shows the resulting single electron identification efficiency as a function of momentum. Figure 4.6 also shows step around $p = 1.4$ GeV/c which is caused by the change of the selection criteria on electron candidates.

4.1.3 Resulting folded J/ψ reconstruction efficiency

Resulting folded J/ψ reconstruction efficiency $\epsilon_{\mathrm{folded}}$ was caculated according to Equation 4.2. Weighting factor, TPC tracking efficiency and geometrical acceptance $\epsilon_{\mathrm{geomxacc}}$ and single electron identification efficiency needed for $\epsilon_{\mathrm{folded}}$ extraction have been described in previous sections. Resulting folded J/ψ reconstruction efficiency can be seen in the right panel of Figure 4.6.

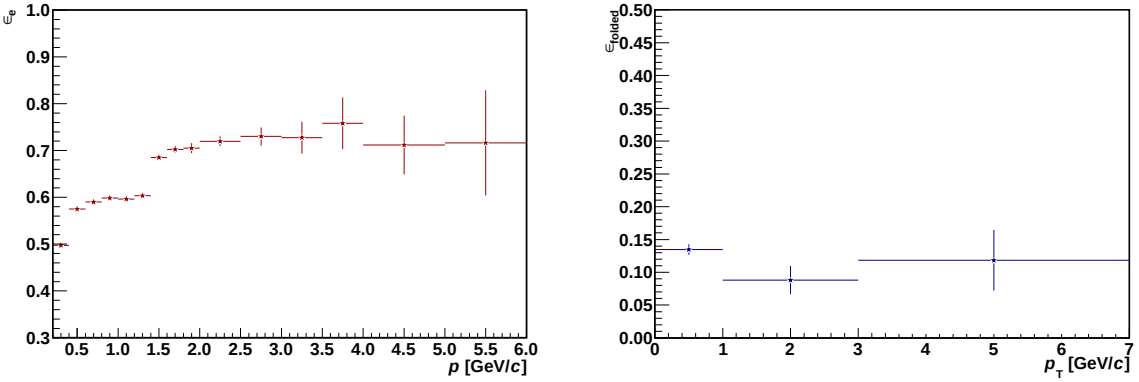

Figure 4.6: Left: Resulting single electron identification efficiency ϵ_e as a function of electron momentum p. Right: Folded J/ψ reconstruction efficiency in three studied transverse momentum bins p_T.

4.2 Signal counting correction

J/ψ signal was calculated by the bin-counting method in the region of electron-positron invariant mass $(2.9, 3.2)$ GeV/c^2. However, due to the detector effects not all of J/ψ are reconstructed in this invariant mass range. The signal counting correction was estimated from the embedding where the simulated J/ψ invariant mass spectra were scaled to the signal peak of the measured spectra. To improve the agreement between the data and the simulation, the correction to the simulated spectra was performed by smearing the momentum resolution of daughter electrons (positrons). This can be seen in left panel of Figure 4.7 and the fraction of J/ψ with invariant mass outside the range $(2.9, 3.2)$ GeV/c^2 was calculated. This fraction was then estimated to be $\sim 10\%$ and increases towards higher p_T.

4.3 Overall J/ψ reconstruction efficiency

Resulting J/ψ reconstruction efficiency ϵ_{reco} was calculated using the formula 4.1 and using the calculated efficiency factors from previous sections. ϵ_{reco} as a function of J/ψ p_T is shown in the right panel of Figure 4.7. As can be seen the overall reconstruction efficiency is on the level of 10 %.

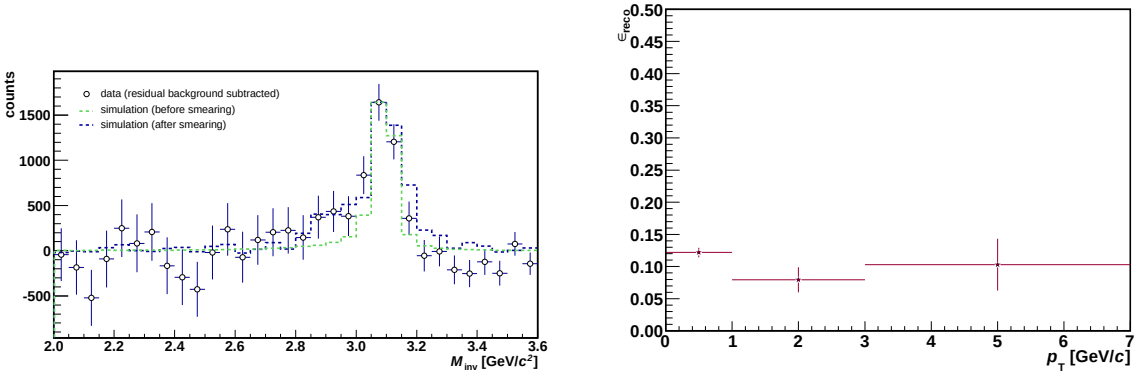

Figure 4.7: Left: J/ψ invariant mass spectrum from data compared to simulation for J/ψ p_T integrated. Right: Resulting J/ψ reconstruction efficiency in three bins of J/ψ p_T.

Chapter 5

Systematic uncertainties

In this chapter the main sources of systematic uncertainties in J/ψ analysis in central U+U data are described. Systematic uncertainties of J/ψ invariant yield coming from the extraction of J/ψ raw yield, simulation and efficiency calculation are evaluated.

5.1 Yield extraction

The J/ψ raw yield was obtained by the bin counting method. First, the combinatorial background was subtracted from the electron-positron invariant mass spectrum. Then, the invariant mass distribution was fitted with the Crystal-Ball function to describe the signal shape and with the linear function to describe the residual background in the range 2.0 - 3.6 GeV/c^2. The uncertainties associated with this method of signal extraction are described below.

Range of bin-counting

One of the contributions to the uncertainty of the yield comes from the choice of the range in which J/ψ signal was counted. The J/ψ raw yield was obtained by counting the number of entries in the electron-positron mass spectrum in the range $2.9 < m_{\mathrm{inv}} < 3.2$ GeV/c^2 after the combinatorial and residual background subtraction. The number of counts was corrected using the fraction of J/ψ outside of this mass range which was determined using the smeared signal shape from simulation.

In order to estimate uncertainty from the range of the bin counting J/ψ raw yield was counted in larger mass window, $2.7 < m_{\mathrm{inv}} < 3.3$ GeV/c^2. Afterwards it was corrected the same way as in the case of smaller range discussed in more detail in Section 4.2 and the difference in the yields was accounted as a systematic uncertainty. It varies in the range 2.8 - 8.1 % depending on p_{T}.

Residual background fitting

Linear function was used to describe the residual background in the invariant mass window $2.0 < m_{\mathrm{inv}} < 3.6$ GeV/c^2. To calculate the corresponding uncertainty other functions were used for the residual background description such as second and third degree polynomials and exponential function. The range of the fit was also varied ($2.0 < m_{\mathrm{inv}} < 3.6$ GeV/c^2, $2.0 < m_{\mathrm{inv}} < 5.0$ GeV/c^2, $2.6 < m_{\mathrm{inv}} < 3.6$ GeV/c^2). Different descriptions of residual background are illustrated in Figure 5.1. It shows the fit of J/ψ mass peak using the Crystal Ball function combined with the listed functions used to describe the residual background. Change of the fitting functions and range caused the difference of the J/ψ yield of 9.4 - 18.1 % depending on p_{T} which was taken as the systematic uncertainty.

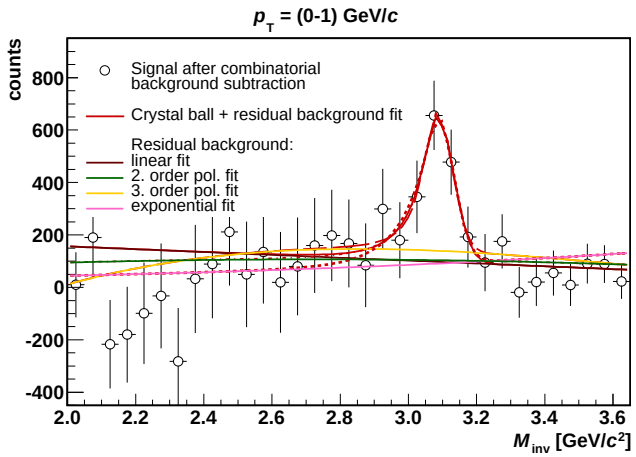

Figure 5.1: Different functions used for the description of the residual background: linear function, second and third degree polynomials and exponential function.

5.2 TPC tracking efficiency and geometrical acceptance

The systematic uncertainty connected with TPC tracking efficiency (Section 4.1.1) and acceptance was estimated from comparing the distributions of number of fitted hits in TPC from simulation and data. As the data the sample of photonic electrons not affected by the requirement on number of fitted hits was used. The method of systematic uncertainty extraction was described in [35]. The fraction of photonic electrons satisfying the requirement on the number of fitted hits (nHitsFit > 19) was calculated. Similar fraction was calculated for the embedded data and the ratio of these two fractions was estimated as the relative uncertainty of the number of fitted hits (in each momentum bin). This uncertainty then propagated to the uncertainty of electron identification and, finally, J/ψ yield and was estimated to be 8.3 - 9.1 % depending on the p_{T} of J/ψ.

5.3 Electron identification efficiency

The single electron identification efficiency consists of TPC cut efficiency, TOF and BEMC cut and matching efficiencies as described in Chapter 4. The systematic uncertainties of these different contributions are described below.

5.3.1 Fitting procedure - range

Constraints on the range of the Gaussian fit of $n\sigma_e$ distributions used for the TPC cut efficiency calculation (Section 4.1.2) were varied to determine the effect on the fitting. The TPC cut efficiency was calculated using different ranges of fitting, $-3.0 < n\sigma_e < 2.0$, $-3.5 < n\sigma_e < 2.5$, $-2.5 < n\sigma_e < 2.0$ and $-4.0 < n\sigma_e < 2.5$. The difference between the highest and lowest values of efficiency was taken as the systematic uncertainty. This accounted for 1.5 - 2.6 %.

5.3.2 Mean and width of the electron Gaussian

Mean and width of the $n\sigma_e$ distributions of photonic electron candidates used for the TPC cut efficiency calculation (Section 4.1.2), see Figure 5.2, are expected to show no momentum dependence. However, due to some calibration effects or remaining hadron contamination under the electron Gaussian there are some contributions to non-constant trend. These effects are more visible in the dependence of Gaussian mean in Figure 5.2.

To take these effects into account, the mean and width of the electron Gaussian were fitted with the constant function in the range $0.2 < p < 6.0$ GeV/c and constant parameters of these fits were used to calculate the TPC cut efficiency. Change of the final yield of J/ψ using the TPC cut efficiency calculated and the TPC cut efficiency calculated using the constant fit described here was estimated to be 1.4 - 1.9 %, and this was accounted as the systematic uncertainty.

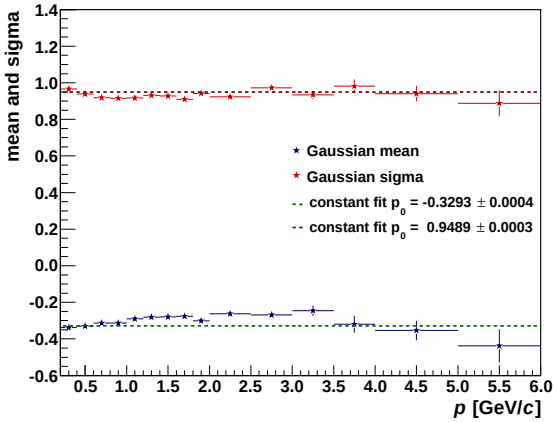

Figure 5.2: Mean and width of the $n\sigma_e$ distributions of photonic electron candidates as a function of photonic electron momentum.

5.3.3 TOF efficiency

TOF cut and matching efficiencies were calculated by comparing the number of photonic electron candidates which satisfied the TOF cut and matching requirements to all of those studied as presented in Section 4.1.2.

TOF matching efficiency

To estimate the systematic uncertainty of the electron TOF matching efficiency, the hadron TOF matching efficiency was calculated. Its momentum dependence was scaled to the calculated electron matching efficiency and the difference between the results of these two calculations was taken as the systematic uncertainty (1.1 - 1.4 %). Figure 5.3 shows the comparison of TOF matching efficiency obtained from electrons and scaled hadrons. This method of TOF matching efficiency calculation was motivated by work [36]. As can be seen the momentum dependence for electrons shows different trend compared with hadrons and will be object for further studies.

TOF cut efficiency

As in[36, 35] the systematic uncertainty of TOF cut efficiency was estimated by using the Gaussian fit of the electron $1/\beta$ distributions. Gaussian fit was used for $1/\beta$ fitting. The area under the Gaussian fit in the TOF cut range $0.970 < 1/\beta < 1.025$ was calculated as well as the area under Gaussian fit in the range $0.93 < 1/\beta < 1.07$. The TOF cut efficiency was then calculated as the ratio of these two areas. $1/\beta$ distribution with Gaussian fit applied is illustrated in the left panel of Figure 5.4. The TOF cut efficiency extracted from data was compared to that obtained from the Gaussian fit. This can be seen in the right panel of Figure 5.4 showing the $\epsilon_{\mathrm{TOFcut}}$ as a function of momentum extracted from bin counting and from fitting. The difference between them caused the difference in the final yield of 1.1 - 1.4 % which was taken as the systematic uncertainty.

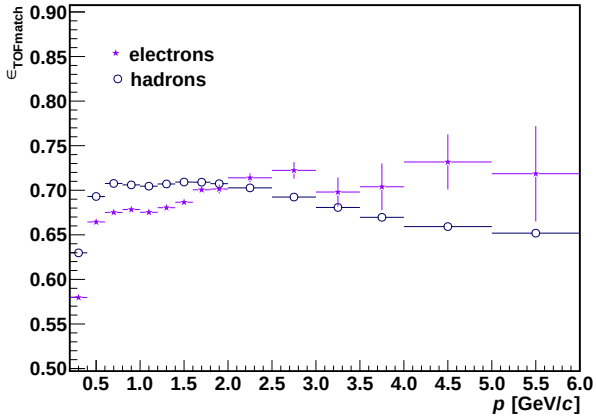

Figure 5.3: TOF matching efficiency for electrons and hadrons as a function of momentum.

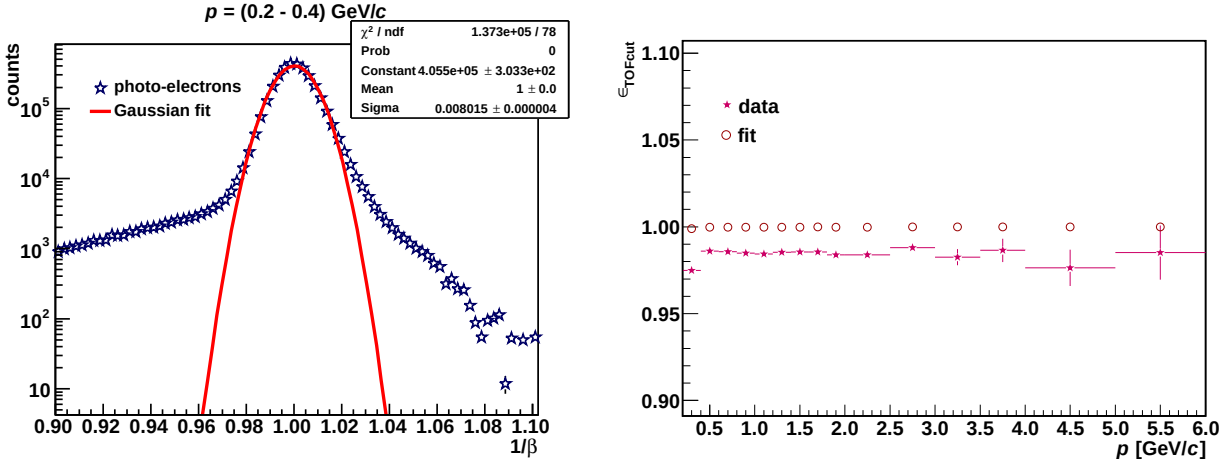

Figure 5.4: Left: $1/\beta$ of photonic electron candidates with momenta 0.4 - 0.6 GeV/c fitted with the Gaussian function. Right: TOF cut efficiency ϵ_{TOFcut} as a function of photonic electron momentum p extracted from data and Gaussian fit.

5.3.4 BEMC efficiency

BEMC cut and matching efficiencies were calculated in a similar way as the TOF efficiencies as described in Section 4.1.2. Below the calculations of corresponding systematic uncertainties are described.

BEMC matching efficiency

The systematic error of BEMC matching efficiency was obtained from comparing the results from data and from simulation. This is illustrated in the Figure 5.5. As can be seen, results from simulation underestimate results obtained from the data analysis. The difference between simulated BEMC matching efficiency and the matching efficiency extracted from data which is 2.9 - 3.9 % was taken as the systematic uncertainty.

BEMC cut efficiency

Similarly to BEMC matching efficiency, BEMC cut efficiency was extracted from data. To estimate the corresponding systematic error it was compared to the BEMC cut efficiency obtained

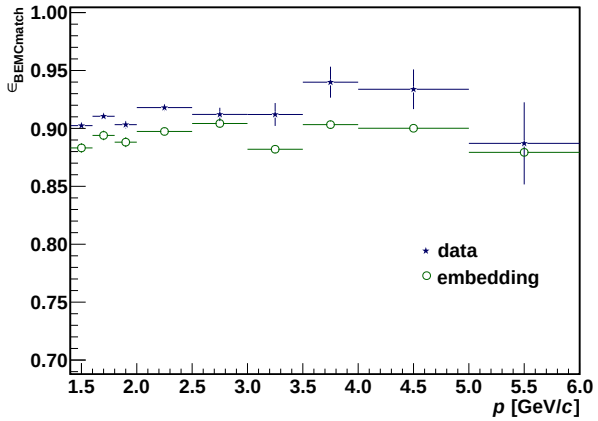

Figure 5.5: BEMC matching efficiency extracted from data and from simulation as a function of electron momentum.

from simulated data. Figure 5.6 shows the pc/E of photonic electrons compared to simulated data from embedding. As can be seen there is a good agreement between the data and the simulation. The resulting BEMC cut efficiency for real and embedded data can be seen in the right panel of Figure 5.6. The difference between $\epsilon_{\mathrm{BEMCcut}}$ for data and simulation resulted in the systematic uncertainty of the J/ψ yield 2.2 - 4.1 % depending on p_{T}.

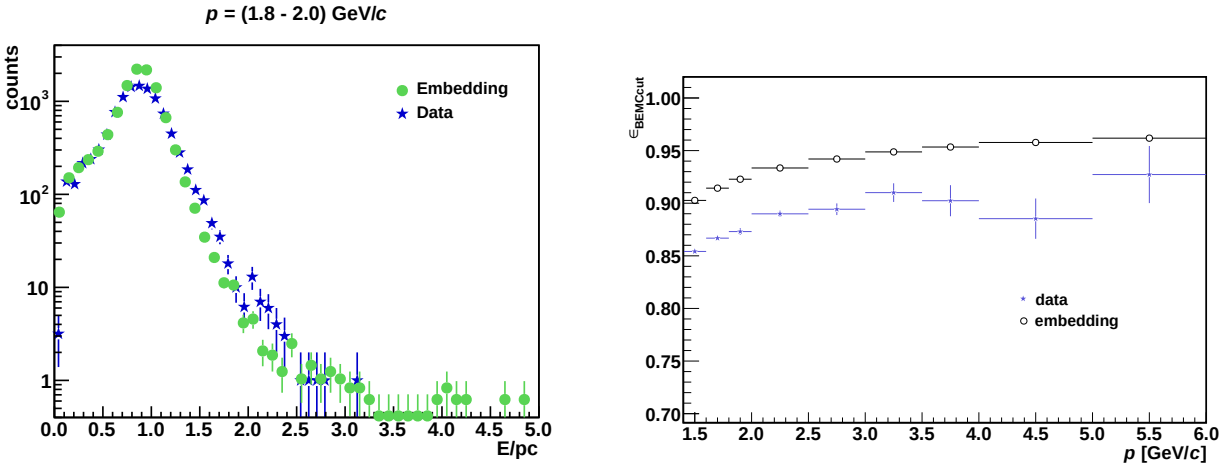

Figure 5.6: Left: pc/E distribution of real and simulated data for electron momentum 1.8 - 2.0 GeV/c. Right: BEMC cut efficiency extracted from data and from simulation as a function of electron momentum.

5.4 Efficiency

Usually, the contributions of single electron identification efficiency are extracted from simulation or estimated as the average between the simulation and data. This method of efficiency calculation enables to reduce statistical fluctuations observed in real data and thus decrease the statistical error of the final results. In the analysis presented in this work, the contributions of single electron identification efficiency were, however, calculated from data, since there were no simulated data for U+U collisions available at the time when this analysis was being performed. The closest possible simulated data for Au+Au from year 2011 were temporarily used instead

of U+U. However, they are different collision system, do not reach as high multiplicities as central triggered U+U and also there could have been some differences in the experimental setup. Hence, a decision was made to temporarily favor the data in the efficiency studies.

As a consequence the obtained results are significantly affected by large statistical uncertainties of efficiency contributions. These are summarized in the in the overall efficiency uncertainty. It was calculated from statistical uncertainties of the electron (positron) identification efficiencies and J/ψ tracking efficiency shown in Chapter 4. These were combined and resulted in the most significant contribution of systematic uncertainty of the yield which varied from 5.9 to 34.8%.

5.5 Resulting systematic uncertainty

The different contributions to resulting systematic uncertainty of J/ψ in 0-5% central U+U collisions as a function of J/ψ transverse momentum are summarized in Table 5.1. As in [36], for the calculation of the total systematic uncertainty all were added in quadratures. Since some of listed contributions are correlated, the resulting systematic uncertainty gives the upper limit of the uncertainty.

J/ψ p_{T} [GeV/c]	0-1	1-3	3-7
Yield extraction			
Range of bin counting	6.6%	2.8%	8.1%
Residual background fitting	18.1%	17.1%	9.4%
TPC tracking efficiency and acceptance	9.1%	8.4%	8.3%
Electron identification efficiency			
TPC cut efficiency (range of fit)	1.5%	1.9%	2.6%
TPC cut efficiency (mean and width)	1.4%	1.8%	1.9%
TOF matching efficiency	1.1%	1.3%	1.4%
TOF cut efficiency	2.1%	2.4%	2.5%
BEMC matching efficiency	3.0%	2.9%	3.9%
BEMC cut efficiency	2.2%	2.6%	4.1%
Efficiency (statistical uncertainty)	5.9%	22.8%	34.8%
Overall uncertainty	22.6%	30.3%	38.4%

Table 5.1: Overview of different sources of systematic uncertainties for different p_{T} bins. These sources are described in more detail in text. Overall uncertainty includes all uncertainties stated above added in quadratures.

Chapter 6

Results

In this chapter the main results of the analysis of J/ψ in 0-5 % central U+U collisions at $\sqrt{s_{\rm NN}}$ = 193 GeV are presented, particularly J/ψ invariant yield and nuclear modification factor.

6.1 Invariant yield

To obtain the invariant yield of J/ψ in 0-5 % central U+U collisions the J/ψ raw yield was corrected on the total reconstruction efficiency (Chapter 4) and normalized to the phase space and the number of events analyzed. The invariant J/ψ $p_{\rm T}$ spectrum is defined as

$$B\frac{d^2N}{d\phi p_{\rm T} dp_{\rm T} dy} = \frac{1}{2\pi p_{\rm T}\Delta p_{\rm T}\Delta y}\frac{N_{J/\psi}}{\epsilon_{\rm total}}\frac{1}{N_{\rm ev}} \tag{6.1}$$

where B denotes the branching ratio $J/\psi \to e^+e^-$, $p_{\rm T}$ is the the mean transverse momentum in a bin of width $\Delta p_{\rm T}$ and the rapidity interval is $\Delta y = 2$ for $|y| < 1$. $N_{J/\psi}$ is the J/ψ raw yield in a given $p_{\rm T}$ bin (Chapter 3), $\epsilon_{\rm total}$ is the total J/ψ reconstruction efficiency discussed in Section 4.3 and $N_{\rm ev}$ is the number of events analyzed satisfying the event cuts (ca. 56 M). Left panel of Figure 6.1 shows the resulting J/ψ invariant yield as a function of the weighted average of $p_{\rm T}$ in given bin. Statistical and systematic uncertainties are also depicted. The yield decreases towards higher $p_{\rm T}$ and for the highest $p_{\rm T}$ the decrease is the most significant.

6.2 Nuclear modification factor

Nuclear modification factor of J/ψ as a function of $p_{\rm T}$ was calculated according to

$$R_{\rm AA}(p_{\rm T}, y) = \frac{1}{< N_{bin} > 0.964/\sigma^{\rm pp}_{\rm inel}}\frac{d^2N_{\rm AA}/dp_{\rm T}dy}{d^2\sigma_{\rm pp}/dp_{\rm T}dy} \tag{6.2}$$

where $d^2N_{\rm AA}/dp_{\rm T}dy$ denotes J/ψ invariant yield in U+U collisions defined above, $< N_{\rm bin} > \sim$ 1172 is the average number of binary nucleon-nucleon collisions in 0–5% central U+U collisions (see Chapter 4). $\sigma^{\rm pp}_{\rm inel}$ is p+p inelastic cross section and U+U collisions 193 GeV and $d^2\sigma_{\rm pp}/dp_{\rm T}dy$ is the invariant cross section of J/ψ production in p+p collisions. The scaling factor 0.964 was included to account for the difference between the charm cross section in p+p collisions at 200 GeV and 193 GeV.

Since STAR lacks J/ψ low-$p_{\rm T}$ data in p+p collisions, and to make the results of this J/ψ analysis consistent with those from minimum bias U+U collisions, the same p+p reference was used, specifically the data from PHENIX [37] (for $p_{\rm T} < 2$ GeV/c) and STAR [13] (for $p_{\rm T} > 2$ GeV/c). The p+p reference fitted with the function 4.3 is shown in the right panel of

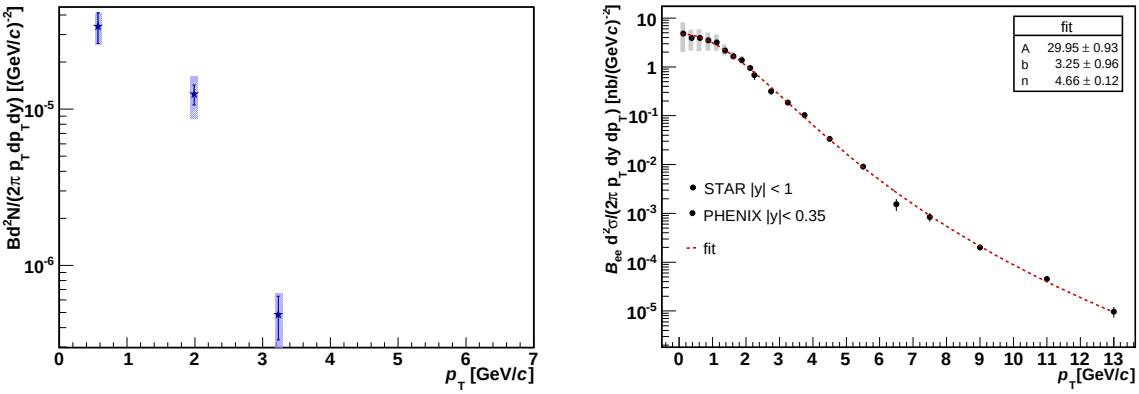

Figure 6.1: Left: J/ψ invariant yield in 0-5 % most central U+U collisions according to TOF+ZDC triggers as a function of transverse momentum p_{T}. Shaded band shows systematic uncertainty of the yield. Right: Proton+proton reference data from STAR [13] (stars) and PHENIX [37] (circles) fitted with the function 4.3.

Figure 6.1. The fitting function was evaluated in the average p_{T} of each J/ψ p_{T} bin and this value was used in formula 6.2.

The resulting J/ψ R_{AA} in 0-5 % most central U+U collisions at STAR calculated according to equation 6.2 can be seen as the function of p_{T} in the right panel of Figure 6.2. It shows significant suppression over the whole p_{T} range. For p_{T} below 3 GeV/c the R_{AA} is similar to results from minimum bias and HT triggered collisions.

J/ψ R_{AA} as a function of N_{part} is shown in the left panel of Figure 6.2. U+U central point is compared to results from minimum-bias U+U collisions and results from Au+Au collisions for $p_{\mathrm{T}} < 5$ GeV/c [13] and $p_{\mathrm{T}} > 5$ GeV/c [14]. A significant N_{part} uncertainty of J/ψ R_{AA} in central U+U collisions (discussed in Chapter 3) is also illustrated. As can be seen J/ψ R_{AA} in central U+U collisions shows significant suppression which is similar to the suppression observed for low-p_{T} J/ψ in 200 GeV Au+Au collisions of $N_{\mathrm{part}} \approx 350$.

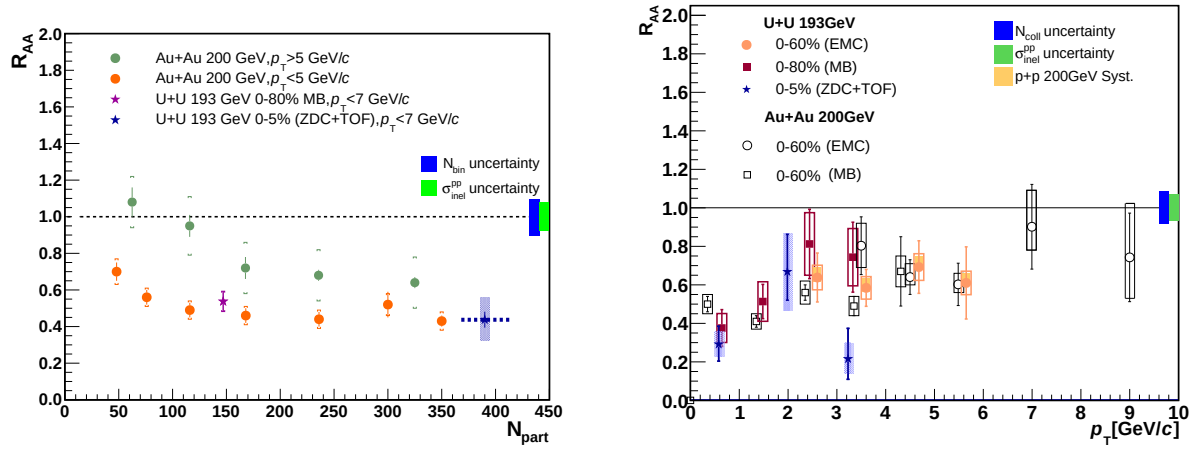

Figure 6.2: J/ψ nuclear modification factor as a function of p_{T} (left) and N_{part} (right) in 0-5 % most central U+U collisions. Data are shown together with minimum bias and HT-triggered Au+Au [14, 13] and U+U data [17]. Shaded band shows systematic uncertainty of the yield and horizontal dashed line shows the systematic uncertainty of N_{part}.

Conclusions

In this work the analysis of J/ψ production via the di-electron decay channel in central triggered 0-5 % most central U+U collisions at $\sqrt{s_{\mathrm{NN}}} = 193$ GeV at the STAR experiment was presented.

Suppression of J/ψ production in heavy-ion collisions compared with p+p collisions provides one of the key signatures of the quark-gluon plasma formation. In U+U collisions the effects of the hot medium are expected to be the most significant among all nuclei which have been collided at RHIC until now. Therefore, J/ψ production studies in such colliding system are important.

The work discusses theoretical prediction of J/ψ production and its modification in heavy-ion collisions as well as recent J/ψ measurements in heavy-ion collisions at RHIC.

One of the foremost heavy-ion experiments, the STAR experiment at RHIC, was presented. Information obtained from three of its main subsystems, the Time Projection Chamber, Time Of Flight detector and Barrel Electromagnetic Calorimeter was used for identification of J/ψ daughter electrons and positrons in central U+U collisions. J/ψ raw yield of significance larger than 8 σ was observed for $p_{\mathrm{T}} < 7$ GeV/c at mid-rapidity. This allowed to divide the signal in three p_{T} bins. Different, either data-driven corrections or corrections based on simulation of J/ψ decay and the interaction of its daughter electrons in the detector were performed. The total J/ψ reconstruction efficiency was estimated to be 8 - 12 % depending on p_{T}. The first estimate of systematic uncertainties was also performed.

Finally, J/ψ invariant yield was calculated and compared to the scaled p+p reference to determine the nuclear modification factor R_{AA}. J/ψ R_{AA} as a function of p_{T} and N_{part} shows significant suppression. J/ψ R_{AA} for $p_{\mathrm{T}} < 3$ GeV/c in central triggered U+U collisions is similar to that observed in minimum bias U+U and Au+Au collisions at 200 GeV at STAR. Our results on J/ψ R_{AA} in central U+U collisions move the centrality studies of J/ψ production in heavy-ion collisions towards higher N_{part}. J/ψ R_{AA} in U+U collisions is consistent with Au+Au results with similar N_{part} indicating possible interplay of dissociation and recombination of heavy quark-antiquark pairs as processes modifying J/ψ production.

Results of J/ψ analysis in central triggered U+U collisions presented in this work are not final. In the future more precise study of J/ψ signal corrections and systematic uncertainties using the simulation for U+U collisions will be performed.

Bibliography

[1] S. Bethke. The 2009 World Average of alpha(s). *Eur. Phys. J.* C **64**, 689-703 (2009).

[2] E. Eichten, K. Gottfried, T. Kinoshita, K. D. Lane, and T. M. Yan. Charmonium: Comparison with experiment. *Phys. Rev.* D **21**, 203–233 (1980).

[3] H. Satz S. Sarkar and B. Sinha. *The Physics of the Quark-Gluon Plasma A: Introductory Lectures*. Springer, Berlin Heidelberg, 1st edition, 2010.

[4] Z. Del Vecchio. Moti collettivi (flow) in collisioni di ioni pesanti. `http://slideplayer.it/slide/619101/`. [online] [05.04.2016].

[5] F.S. Bieser *et al.* The STAR trigger. *Nuclear Instruments and Methods in Physics Research Section A: Accelerators, Spectrometers, Detectors and Associated Equipment*, **499**(2-3). 766–777 (2003).

[6] T. Schuster M. Kliemant, R. Sahoo and R. Stock. Global properties of nucleus–nucleus collisions. In *The Physics of the Quark-Gluon Plasma*, volume 785 of *Lecture Notes in Physics*, pages 23–103. Springer, Berlin Heidelberg, 2010.

[7] E. V. Shuryak. High-energy collisions of strongly deformed nuclei: An Old idea with a new twist. *Phys. Rev.*, C **61**. 034905 (2000).

[8] G. Odyniec D. Kikola and R. Vogt. Prospects for quarkonia production studies in U + U collisions. *Phys. Rev.*, C **84**. 054907 (2011).

[9] T. Matsui and H. Satz. J/ψ Suppression by Quark-Gluon Plasma Formation. *Phys.Lett.*, B **178**. 416 (1986).

[10] A. Mócsy and P. Petreczky. Can quarkonia survive deconfinement? *Phys. Rev.*, D **77**. 014501 (2008).

[11] H. Pereira Da Costa. Charmonium production in Pb-Pb collisions with ALICE at the LHC. arXiv 1512.07610 (2015).

[12] N.Xu Y. Liu, Z. Qu and P. Zhuang. J/ψ Transverse Momentum Distribution in High Energy Nuclear Collisions at RHIC. *Phys. Lett.*, B **678**, 72–76 (2009).

[13] L. Adamczyk et al. J/ψ production at low p_T in Au+Au and Cu+Cu collisions at $\sqrt{s_{NN}} =$ 200 GeV with the STAR detector. *Phys. Rev.*, C **90**(2), 024906 (2014).

[14] L. Adamczyk et al. J/ψ production at high transverse momenta in $p + p$ and Au+Au collisions at $\sqrt{s_{NN}} = 200$ GeV. *Phys. Lett.*, B **722**. 55–62 (2013).

[15] A. Adare *et al.* J/ψ Production vs Centrality, Transverse Momentum, and Rapidity in Au+Au Collisions at $\sqrt{s_{NN}} = 200$ GeV. *Phys. Rev. Lett.*, **98**, 232301 (2007).

[16] X. Zhao and R. Rapp. Charmonium in Medium: From Correlators to Experiment. *Phys. Rev.*, C **82**. 064905 (2010).

[17] W. Zha. Recent measurements of quarkonium production in $p + p$ and A + A collisions from the STAR experiment. *Nucl. Phys.*, A **931**. 596-600 (2014).

[18] Brookhaven National Laboratory. The STAR experiment at the Relativistic Heavy Ion Collider. `http://www.star.bnl.gov/`. [online] [31.03.2016].

[19] W. Fischer. Run overview ofthe Relativistic Heavy Ion Collider. `http://www.rhichome.bnl.gov/RHIC/Runs/`. [online] [10.04.2016].

[20] Brookhaven National Laboratory. The RHIC Complex. `https://www.bnl.gov/rhic/complex.asp`. [online] [31.03.2016].

[21] Brookhaven National Laboratory. PHENIX A Physics Experiment At RHIC. `http://www.phenix.bnl.gov/`. [online] [31.03.2016].

[22] M. Anderson, J. Berkovitz, W. Betts, R. Bossingham, F. Bieser, et al. The STAR Time Projection Chamber: A Unique tool for studying high multiplicity events at RHIC. *Nucl. Instrum. Meth.*, A **499**. 659–678 (2003).

[23] The STAR Collaboration. A Proposal for STAR Inner TPC Sector Upgrade (iTPC). `http://indico.cern.ch/event/30248/session/49/contribution/253/material/slides/0.pdf`. [online] [08.06.2015].

[24] H. Bichsel. A method to improve tracking and particle identification in tpcs and silicon detectors. *Nuclear Instruments and Methods in Physics Research Section A: Accelerators, Spectrometers, Detectors and Associated Equipment*, **562**(1). 154–197 (2006).

[25] STAR detector overview. *Nuclear Instruments and Methods in Physics Research Section A: Accelerators, Spectrometers, Detectors and Associated Equipment*, **499**(23). 624–632 (2003).

[26] The STAR TOF Collaboration. Proposal for a Large Area Time of Flight Sytem for STAR. `https://www.star.bnl.gov/public/tof/`, 2004.

[27] K.A. Olive *et al.* (Particle Data Group), *Chin. Phys.* C **38**, 090001 (2014) and (2015) update.

[28] M. Shao, O. Barannikova, X. Dong, Y. Fisyak, L. Ruan, et al. Extensive particle identification with TPC and TOF at the STAR experiment. *Nucl.Instrum.Meth.*, A **558**. 419–429 (2006).

[29] T.M. Cormier, A.I. Pavlinov, M.V. Rykov, V.L. Rykov, and K.E. Shestermanov. STAR Barrel Electromagnetic Calorimeter absolute calibration using 'minimum ionizing particles' from collisions at RHIC. *Nucl.Instrum.Meth.*, A **483**. 734–746 (2002).

[30] STAR Collaboration. SketchUp STAR. `https://drupal.star.bnl.gov/STAR/subsys/bemc`. [online] [20.10.2015].

[31] J. P. Whitfield. Level 0 Simulation Analysis, Introduction. `https://www.star.bnl.gov/public/trg/GeneralTrigger/Simulations/level_0/level0_intro.html`.

[32] A. Denisov C. Adler, H. Strobele E. Garcia, M. J. Murray, and S. N. White. The RHIC Zero Degree Calorimeter. *Nucl. Instrum. Meth.*, A **470**, 488–499 (2001).

[33] S. Chatrchyan et al. Suppression of non-prompt J/ψ, prompt J/ψ, and Y(1S) in PbPb collisions at $\sqrt{s_{NN}} = 2.76$ TeV. *JHEP*, **05**. 063 (2012).

[34] A. Adare *et al.* Ground and excited state charmonium production in $p + p$ collisions at $\sqrt{s} = 200$ GeV. *Phys. Rev.*, D **85**. 092004 (2012).

[35] W. Zha. J/ψ production in Au+Au collisions at $\sqrt{s_{\rm NN}}$ = 39, 62.4 and 200 GeV. STAR Analysis note. 2015.

[36] C. B. Powell. J/ψ Production in Heavy Ion Collisions at the STAR Detector at RHIC. PhD Thesis. 2012.

[37] A. Adare *et al.* Transverse-momentum dependence of the J/ψ nuclear modification in d+Au collisions at $\sqrt{s_{NN}} = 200$ GeV. *Phys. Rev.*, C **87**. 034904 (2013).